INFORMATION TO USERS

Earth orbiting objects observed by the infrared astronomical satellite

Dow, Kimberly Lynn, M.S.

The University of Arizona, 1992

U·M·I
300 N. Zeeb Rd.
Ann Arbor, MI 48106

EARTH ORBITING OBJECTS OBSERVED BY THE INFRARED

ASTRONOMICAL SATELLITE

by

Kimberly Lynn Dow

A Thesis Submitted to the Faculty of the

DEPARTMENT OF ASTRONOMY

In Partial Fulfillment of the Requirements
For the Degree of

MASTER OF SCIENCE

In the Graduate College

THE UNIVERSITY OF ARIZONA

1992

STATEMENT BY AUTHOR

This thesis has been submitted in partial fulfillment of the requirements for an advanced degree at the University of Arizona and is deposited in the University Library to be made available to borrowers under rules of the Library.

Brief quotations from this thesis are allowable without special permission, provided that accurate acknowledgment of source is made. Requests for permission for extended quotation from or reproduction of this manuscript in whole or part may be granted by the head of the Astronomy Department or the Dean of the Graduate College when in his or her judgment the proposed use of the material is in the interest of scholarship. In all other instances, however, permission must be obtained from the author.

SIGNED: *Kimberly Ann*

APPROVAL BY THESIS DIRECTOR

This thesis has been approved on the date shown below:

F. J. Low
Professor of Astronomy

June 10, 1992
Date

DEDICATION

to my family

ACKNOWLEDGMENT

I am grateful for the technical assistance that I received from several individuals with whom I have had the pleasure to collaborate. At the Lockheed Engineering and Management Company, Rich Rast and Phil Anz-Meador provided invaluable information concerning the space debris population. Sincere thanks are also due to Dave Harvey, one of the kindest, most considerate people that I have had the privilege to meet at Steward, whose knowledge of the Air Force software SATRAK made it possible to correlate the Earth orbiting objects observed by IRAS with known artificial satellites.

I am also thankful to Mark Sykes for giving me the opportunity to come to the University of Arizona and for sending me to conferences to present the results of my work. Warmest appreciation to Marcia Rieke for her consistent support during this project. Thanks also to Frank Low for inspiring me to pursue worthwhile collaborations at other astronomical institutions.

Deepest gratitude to the gang at Snoopy's Flight School, especially Scott Genzman and Jason Danof, who not only taught me the finer points of flying but who continued to rent me airplanes even after I repeatedly tried to confound the Ryan Airfield control tower, other pilots and probably the local bird population.

I feel fortunate to have been able to call Liz Alvarez, Cathy and Dan Clemens, Dave Harvey, Todd Henry, Davy Kirkpatrik, Don McCarthy, Jeff Regester, Simon White, Connie Walker and Grace Wolf my friends. Thank you for offering your comic relief and support when I needed it the most.

I would also like to thank Geraint Lewis, Jenny McDonald, Peter Tribble, Derek Richardson and Ted von Hipple of the Institue of Astronomy at the University of Cambridge who made me feel so at home while finishing this thesis and for giving me three of the happiest months of my graduate career.

Lastly, to the Peking Restaurant for the inspiration received from a fortune cookie I opened shortly after arriving in Tucson which read "a great pleasure in life is doing what others say you can't."

TABLE OF CONTENTS

LIST OF FIGURES

LIST OF TABLES

ABSTRACT

A systematic search (Dow and Sykes 1988) for cometary dust trails (Fig. 1) in the Infrared Astronomical Satellite (IRAS) Sky Brightness Images (IRAS Sky Brightness Images 1988) resulted in the discovery of 466 sources (Dow *et al.* 1990) that are not in the IRAS Point Source Catalog (IRAS Point Source Catalog, Version 2 1988) or in the Small Scale Structure Catalog (IRAS Small Scale Structure Catalog 1988). Nearly all of the sources that were found are best explained as artificial satellites or pieces of Earth orbiting debris. In this paper the term "artificial satellite" refers to an active payload. Orbital debris, or equivalently space debris, is defined as any non-operational object in space.

This study addresses two questions. To what degrees have the Sky Brightness Images (hereafter, also referred to as Images) been contaminated by orbital debris, given that the IRAS detectors were well suited and that the satellite was well positioned to observe these sources? Second, can valuable information concerning the thermal characteristics of these sources be obtained by suitably analyzing IRAS data?

Fifty-four sources, covering a range of positions and observed fluxes, were selected from the main sample to determine their angular motion, flux density and color temperature distributions. Four of these objects were correlated with known artificial satellites.

INTRODUCTION

IRAS was launched on 26 January 1983, as a joint mission by the United States, the Netherlands and the United Kingdom. The main purpose of the mission was to perform an unbiased, highly sensitive and reliable survey of the sky in four broad wavelength bands, centered roughly at 12, 25, 60 and 100 μm (band 1, 2, 3 and 4), and to generate a catalog of infrared point sources.

The mission was designed to perform three complete surveys of the sky during the satellite's anticipated one-year lifetime. The intent of this strategy was not to improve the sensitivity of the survey but rather to increase the reliability of astrophysical point sources in the presence of moving sources such as space debris, energetic particles and asteroids.

In spite of telescope design and data processing efforts, non-astronomical sources of infrared radiation (material emitted by IRAS, Earth orbiting satellites and space debris) were detected. Moving astronomical objects, including natural meteoroids, comets, asteroids and energetic particles, were also observed by IRAS. Evidence for the presence of these sources was found in the IRAS Sky Brightness Images and in the Calibrated Reconstructed Detector Data (CRDD). The Sky Brightness Images collectively comprise an atlas, available as photographs or on magnetic tape in digital form, of the entire infrared sky at wavelengths corresponding to the IRAS passbands. The CRDD is a data base that lists, by detector, ADUs as a function of the sampling rate. It can also be viewed graphically as strip charts. The flux density, inclination and angular motion of an object as well as the date and time of the observation can be determined from the CRDD.

Several studies have demonstrated the ability of IRAS data to characterize infrared emission from orbital debris. DeJong and Wesselius (1990), Anz-Meador *et al.* (1986) and Walsh *et al.* (1989) have used search procedures, primarily using unprocessed IRAS detector data, to search for debris. While their studies have found a few moving sources, some of which are below the flux limit of the Sky Brightness Images, they are essentially blind searches through many hours of the detector data that covered only a few days of the mission.

In this study, however, objects were found on the Sky Brightness Images over the entire duration of the IRAS mission. The signature of an Earth orbiting object (Fig. 2) was distinct and easily identified when Images corresponding to bands 1, 2 and 3 were overlaid. While potentially thousands of much fainter sources may be found in the IRAS data bases by other investigators, the objects found using the Sky Brightness Images and the CRDD will be the brightest moving sources detected by IRAS and will provide a large sample of sources to examine.

The IRAS mission offered a unique opportunity to observe, with a large space-based telescope, the small-sized debris population and to learn something about the thermal properties of debris in several size regimes. Analysis of the IRAS detection capabilities indicated that the satellite's 12 μm detectors could observe an object with a diameter of one centimeter at a range of 400 kilometers, and an object with a diameter of 10 centimeters at a range of 4000 kilometers. Comparatively, ground-based observations at visible wavelengths are currently capable of detecting debris with diameters a few to 10 centimeters out to low Earth orbit (LEO), altitudes lower than 2000 kilometers, and as small as one meter in geosynchronous orbit (GEO). Ground-based infrared observations with the MOTIF B telescope on the island of Maui are even worse, having a resolution of one square meter in LEO (Vilas 1992). It has been estimated that as many as 80000 objects

with diameters as small as one centimeter are not tracked by ground-based radars and optical systems (Johnson and McKnight 1987).

Designers of future missions must consider not only protection from bright pieces of debris confusing fine-guidance sensors (which already happened to the Solar Max payload, Anz-Meador 1992) or damaging electronic equipment, but also debris collision avoidance techniques and the probability of debris particles impacting the spacecraft with sufficient energy to fragment the payload. Space-based astronomical telescopes must also contend with paint flakes and dust collecting on mirror surfaces, thereby degrading imaging ability.

Plans by NASA for a permanent manned space station have resulted in increased concern about the characterization and detection of debris in LEO. The Debris Collision Warning Sensor (DCWS) flight experiment (Vilas 1992) will be the first space-based mission optimized for the detection of space debris. This data will contribute to studies in preparation for this flight experiment.

Chapter One describes the IRAS mission and the final data products that are relevant to this project. In Chapter Two, the IRAS Moving Source and Cometary Dust Trail Survey search procedure is presented and the characteristics of some of the sources which were observed are also described. Chapter Three discusses what is currently understood about the orbital debris environment and how the results of this project may contribute to those perceptions.

IRAS Multiple Band Sky Brightness Image
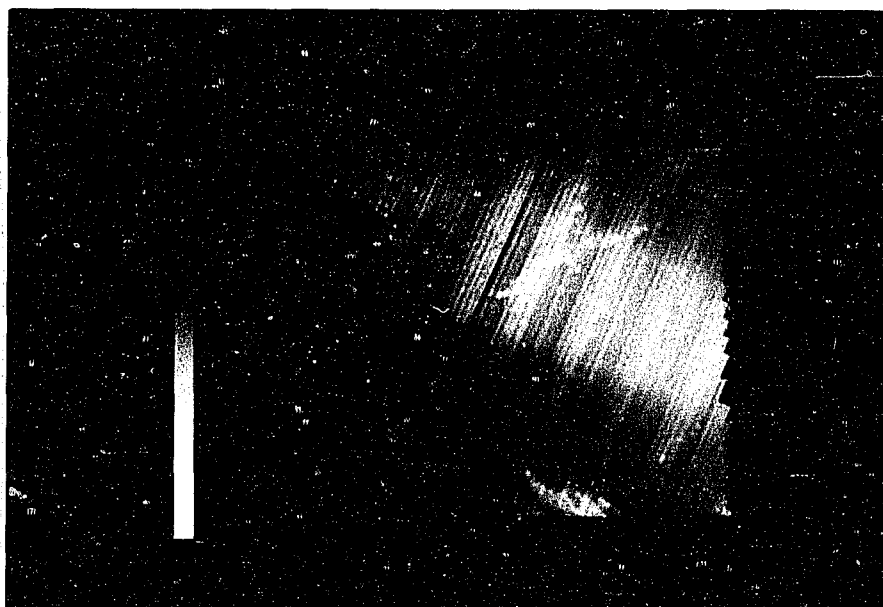
Figure 1: This is a multiple band Sky Brightness Image that is centered at 0^h right ascension and 0° declination (1950), geocentric. The image is color coded according to passband: band 1 is blue; band 2 is green and band 3 is red. North is to the top and east is to the left. The wide structure passing through the image is an asteroid dust band that contains debris resulting from collisions between asteroids. A thin dust trail, associated with the perihelion passage of comet Temple 2, is seen cutting through the image to the south of the dust band. A dust trail associated with the comet Encke is north of the dust band. The wispy features are galactic cirrus. All of these structures were discovered by IRAS.

Earth Orbiting Source on IRAS Sky Brightness Image
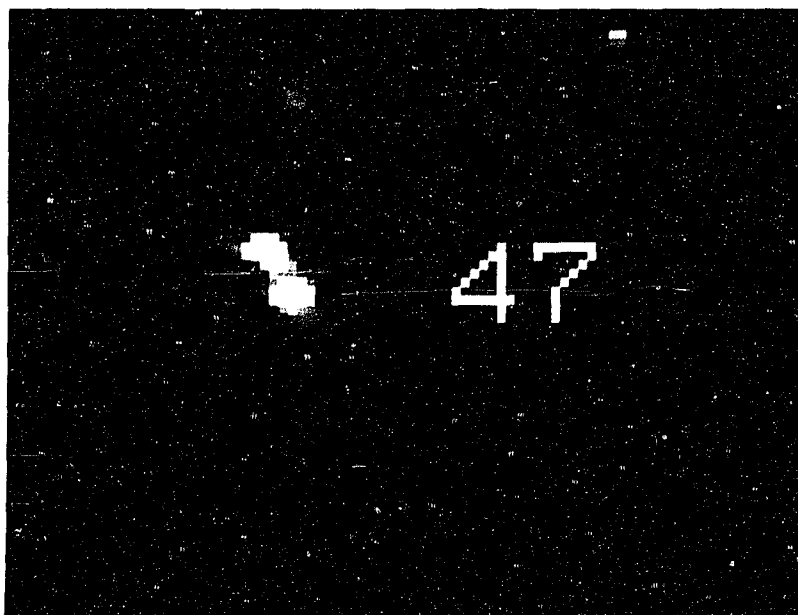
Figure 2: This is the signature of a typical Earth orbiting source as seen on an IRAS Sky Brightness Image. The image is color coded by passband as in Figure 1. The position of Source 47 is 13:56:48 +76:04:20. Photographs of other sources are found in Appendix 5.

CHAPTER ONE

Characteristics of the IRAS Mission and Data Bases

1. The IRAS Satellite

The components of the IRAS spacecraft, telescope and focal plane that are relevant to the IRAS Moving Source and Cometary Dust Trail Survey are described in the following two sections. More detailed information about the spacecraft and the mission can be found in the IRAS Explanatory Supplement (IRAS Catalogs and Atlases 1988).

1.1 Spacecraft

The main features of the IRAS spacecraft are the onboard computers and software, the attitude control system and the data recording devices. General characteristics of each of these systems are outlined in the following paragraphs. The spacecraft is more fully described by Pouw (1983) and Neugebauer *et al.* (1984).

IRAS was equipped with two identical computers, each of which had a Central Processing Unit (CPU) with 64 K of Random Access Memory (RAM). The RAM contained the procedures for carrying out a complete Satellite Operations Plan (SOP). The length of a SOP was the amount of time between ground station passes, typically ten to fourteen hours. There were 2 SOPs in a day and 600 SOPs in the entire mission. Each SOP was also referenced by an orbit number, "OBS", of which there were 14 available each day. The RAM also included the routines for initiating the downlink of the data stream to the ground station in Chilton, England. During the downlink, which lasted approximately 10

minutes, instructions for the next SOP were transmitted to the satellite. The order of the SOP/OBS was such that they can be correlated with one of the three all-sky surveys, a feature that proved to be invaluable when trying to locate specific portions of the CRDD.

The attitude of the telescope was controlled by a horizon sensor, a Sun-sensor and three orthogonal gyros. During observations the y-axis gyro was kept perpendicular to the Sun-satellite line, the x-axis indicated the direction in which the boresight of the focal plane array was pointing and the z-axis was pointed toward the Sun (Fig. 3). Visible wavelength star-sensors, located in the telescope focal plane, were used for onboard attitude updates. The star sensors were arranged in a "V" configuration to provide attitude information for two axes. The positional accuracy of sources observed by IRAS depended on their size, spectral energy distribution and brightness, but was typically better than 20 arc-seconds. The reconstructed pointing accuracy, however, was accurate to two or three arc-seconds (Low 1991). This high degree of precision contributed to the ability to correlate sources observed by IRAS with known artificial satellites.

One onboard tape recorder allowed data from the previous SOP to be transmitted to Earth during a ground station pass, while the second recorder simultaneously accepted data for the current SOP. This method protected data from being overwritten when information from a particular SOP could not be downlinked completely during a given ground station pass.

IRAS Orbital Geometry
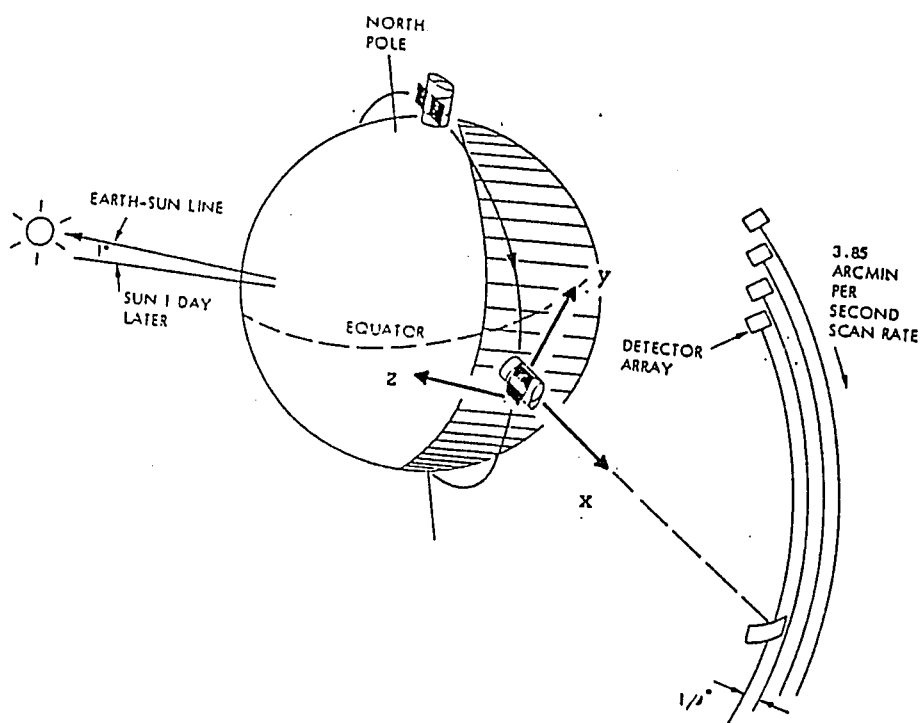
Figure 3: IRAS was in a Sun-synchronous, 103 minute orbit above the Earth's terminator. A series of scans on the celestial sphere is also indicated.

1.2 Telescope and Focal Plane Assembly

The IRAS telescope was a Ritchey-Chretien configuration with a 0.57-meter aperture and a 5.5-meter focal length (Fig. 4). The unvignetted field of view was 63.6 arc-minutes and the plate scale was 1.6 millimeters/arc-minute. The telescope was cooled to temperatures ranging between 2 and 5 K by mounting it in a liquid helium cryostat. The mirror was constructed of beryllium because it is lightweight and has minimal thermal distortion when cooled to cryogenic temperatures. The secondary was beryllium coated with aluminum. The optics of the telescope were protected during launch and during the first week of the mission with an aperture cover cooled with superfluid helium.

The focal plane assembly was located at the Cassegrain focus of the telescope (Fig. 5) and was cooled to 2.6 K. The array consisted of 62 rectangular solid state infrared detectors arranged in linear columns so that all distant astronomical sources, which always passed in front of the focal plane in the image or *in-scan* direction, could be seen by at least two detectors in each of the four bands. Artificial satellites, on the other hand, crossed the focal plane from many directions, including the in-scan direction. The 12 and 25 μm detectors were constructed of Si:As and Si:Sb respectively and the 60 and 100 μm detectors were constructed of Ge:Ga. Three of the 62 detectors were declared inoperable and four were considered degraded. More detailed information pertaining to detector characteristics appears in Table 1.

The responsivity of the detectors, the ratio of the detector current to the power falling on the detector, was monitored by ten thermal calibration sources called "internal reference sources" or "stimulators", mounted behind the secondary mirror. These detectors provided pulses of

IRAS Spacecraft and Telescope System.

COVER
LOW
THRUST
VENT

+X

+Z

+Y

EJECTABLE
APERTURE
COVER

TELESCOPE
AXES
ORIENTATION

SUPERCRITICAL
HELIUM TANK

SUNSHADE

OPTICAL
BAFFLE

SECONDARY
MIRROR

EARTH SHIELD

SUPERFLUID
HELIUM TANK

PRIMARY
MIRROR

EXPERIMENT
ELECTRONICS

FOCAL
PLANE
ASSEMBLY

DUTCH
ADDITIONAL
EXPERIMENT

DUTCH
ADDITIONAL
EXPERIMENT
ELECTRONICS

CRYOGENIC
VALVES AND
MANIFOLD

HORIZON
SENSOR

SPACECRAFT

Figure 4: The dimension of the satellite with deployed solar arrays was 3.60 meters (height), 3.24 meters (width) and 2.05 meters (depth).

IRAS Focal Plane Assembly

WAVELENGTH BANDS, μm
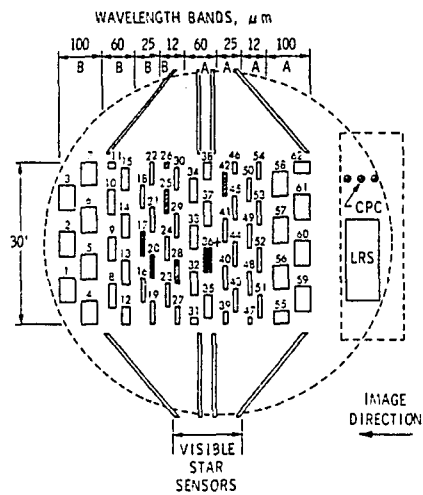
Figure 5: The cross-hatched detectors were degraded and the filled-in detectors were inoperable. The y and z axis of the satellite are indicated at right. The focal plane contains two modules, A and B, as indicated. The CPC was a chopped photometric channel and the LRS was a low resolution spectrometer.

TABLE 1
IRAS Detector Characteristics

band	bandwidth FWHM (μm)	detector FOV (Arcmin.)	detector material	no. of operational detectors	NEFD* 3σ(mJy)	Sampling Rate (sec)	Detector Size (mm)
1	7.0	0.75x4.5	Si:As	16	315	1/16	1x1.78
2	11.5	0.75x4.6	Si:Sb	13	375	1/16	1x1.78
3	32.5	1.5x4.7	Ge:Ga	15	510	1/8	1.5x1.5
4	31.5	3.0x5.0	Ge:Ga	15	1740	1/4	1.25x1.25

* Noise Equivalent Flux Density

infrared radiation before and after each survey scan and were also used with pointed observations. Interestingly, when the Sky Brightness Image positions were matched with the CRDD it was found that three of the 54 sources were correlated with these pulses. This phenomenon is not understood at this time.

2. IRAS Orbital Geometry and Survey Operations

IRAS was launched into a Sun-synchronous orbit at an altitude of 900 kilometers and an inclination of 99°. The orbit of the spacecraft precessed in right ascension at a rate of slightly under one degree per day, (matching the Earth's average revolution rate about the Sun), allowing the plane of its orbit to remain roughly fixed with respect to the Sun. This configuration was chosen to minimize the likelihood of radiation from the Sun and Earth, from entering the telescope, to maximize the effectiveness of the solar panels and to ensure that an all-sky survey was completed within six months. During survey operations, the optics were protected from off-axis emission by a sunshade--provided that the telescope did not point closer than 60° in the direction of the Sun. The attitude control system did not permit the spacecraft to point further than 120° away from the Sun. IRAS was also not permitted to point closer than one degree toward Jupiter or closer than 25° in the direction of the Moon.

During the sky survey, the focal plane scanned a section of the sky that was 0.5° wide. The position of the satellite was shifted near the ecliptic by 14.23 arc-minutes, approximately half of the width of the focal plane, allowing a source observed on one side of the focal plane during one orbit to be observed on the opposite side of the focal plane on the next orbit. As a result, the same location of sky was observed twice over successive orbits. These hours-confirming observations were called "HCONs". During the first

seven months of the mission, a given region of sky was observed for about one week and then re-observed on a time-scale of 7—11 days. The first week was designated HCON 1 and the second week was designated HCON 2. HCONs 1 and 2 each covered 96% of the sky. HCON 3 was completed during the last three months of the mission and covered 76% of the sky. Three sets of Sky Brightness Images were constructed from individual scans corresponding to the three HCONs. The Sky Brightness Images are discussed in greater detail in Chapter Two Section One.

The scan rate of IRAS, 3.85 arc-minutes/second, was faster than the orbital rate, 3.5 arc-minutes/second, to allow for increased pointing flexibility in survey mode and to enable more time to complete the Additional Observation program (Chester 1991). The pointing flexibility also helped to reduce the effects of the South Atlantic Anomaly (SAA),that part of the inner Van Allen radiation belt lying approximately 200 kilometers above the Earth's surface and arising because the Earth's magnetic field is offset from its center by 500 kilometers. Energetic charged particles in the SAA often play havoc with spacecraft components, such as scientific instruments, computers and guidance sensors.

3. Removal of Moving Sources

Many fast moving sources, such as energetic particles and orbital debris, were removed during the IRAS mission by means of an electronic discriminator before the data stream was downlinked to the ground station. Many objects, however, made it past this circuit and were not removed from the Sky Brightness Images until they were found from visual examination of the Images (Gautier 1989) by scientists at the Infrared Processing and Analysis Center (IPAC) in Pasadena, California.

3.1 Onboard De-glitcher

An electronic discriminator, colloquially called the "de-glitcher", was employed to remove from the survey data stream, signals with fast rise times, bright space debris and energetic particles. This procedure was important during passages through the SAA where the radiation dosage was particularly high. Only the largest voltage spikes were "de-glitched", and borderline spikes often were not completely removed. The de-glitcher treated the 12 and 25 μm detections of fast rising signals in the same manner because the detectors were of the same electronic design; therefore, even if the brightest 12 and 25 μm signals were only partly eliminated, it is not important because the ratio of the flux density did not change (Low 1991). This is one of the reasons that the most reliable color temperatures of the brightest sources in this study are determined from the ratio of the 12 and 25 μm fluxes. The primary reason, however, is that most of the flux from any inner solar system object is emitted in the 12 and 25 μm bandpasses. Faint sources, on the other hand, are unlikely to trigger the de-glitcher and should have reliable fluxes in all four bandpasses. The de-glitcher was operated continuously during the mission and may have eliminated many debris events that were observed by IRAS.

3.2 Data Processing of Sky Brightness Images

As a final measure, before their general release to the scientific community, all the Sky Brightness Image fields were visually examined for sources that appeared anomalous. Near-field objects that flooded the focal plane, and 25 μm scans which differed substantially in brightness from adjacent scans, were removed. The later was accomplished by adding a scan back in to the image with the negative of its original weight.

One hundred twenty-three of the most obvious particle hits and 20 radiation hits were removed at IPAC from the Sky Brightness Images. These sources were easily identified because they illuminated the entire focal plane and therefore covered a larger area on a Sky Brightness Image (Fig. 6). In the study described here, only 12 of the 466 sources that were found are obvious "near-field" sources. They were often partially obscured by infrared cirrus, making their visual detection difficult, and were not studied as part of this project. (Cirrus is far infrared emission from dust in the solar system and the Galaxy.)

Summary of Chapter One

While the orbital configuration of the satellite precluded the detection of debris below 900 kilometers, IRAS was an extremely useful instrument, albeit unintentionally, for orbital debris studies. The sensitivity of the United States Space Command (USSPACECOM) ground-based radars decreases above 500 kilometers, which makes IRAS a useful tool for detecting debris. Coincidentally, the spatial density of the entire tracked satellite population is greatest between 800 and 1100 kilometers. Additionally, two of the largest satellite fragmentations to date are an Agena D rocket that launched Nimbus 4 and KOSMOS 1275. The Agena was in an orbit at an inclination of 99.79° when it fragmented on 17 October 1970 and an altitude of 1076 kilometers. The KOSMOS 1275 payload had an orbital inclination of 82.96° when it fragmented on 24 July 1981 at an altitude of 977 kilometers. The Agena rocket created 337 debris fragments and KOSMOS 1275 created 249 fragments that could be detected by USSPACECOM (Johnson and Nauer 1987). Additionally, six Delta rocket second stages fragmented in Sun-synchronous orbits between 905 and 1513 kilometers before the deployment of IRAS. Almost all of this debris is still in orbit and is representative of a larger untracked population. Given this scenario, it would seem that the de-glitcher was effective in one of the most densely populated debris regimes.

Still, users of the Sky Brightness Images should bear in mind that no attempt was made to find or remove non-astronomical point-like sources during the "cleaning" process. Many point-like sources can be found in the Sky Brightness Images that do not appear in the same place in different sky coverages. When examining small point sources on these Images one can easily be fooled, unless at least two Images are compared. These non-confirming sources are generally due to asteroids and orbital debris.

Near Field Source on IRAS Sky Brightness Image
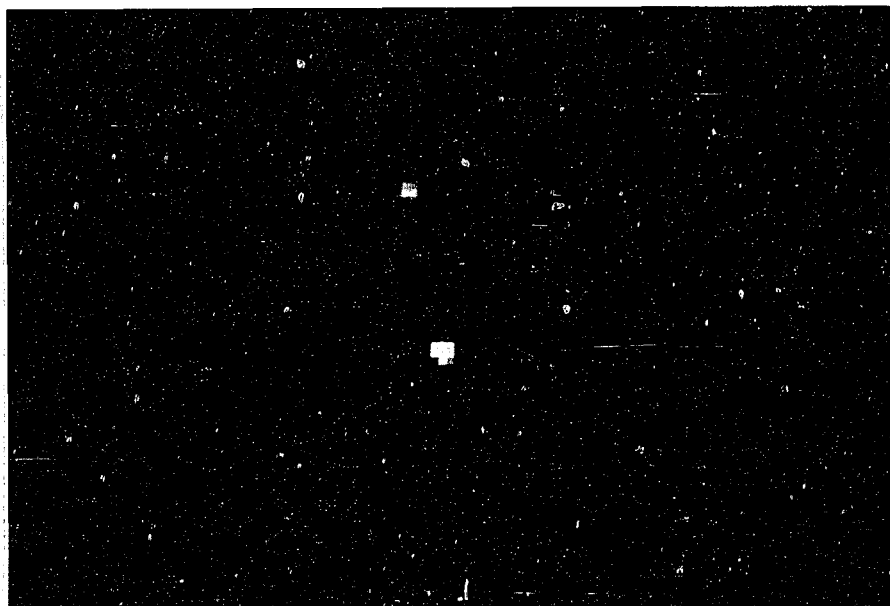
Figure 6: One hundred forty-three near field sources were removed in the data processing before the release of the Sky Brightness Images to the general scientific community. The near-field source seen in this image has illuminated all the detectors in both 12 μm (blue) and 60 μm (red) detector modules. This source passed in front of the focal plane perpendicular to the scan direction. Each point corresponds to a different detector.

CHAPTER TWO

The Search for Moving Sources in the IRAS Sky Brightness Images

1. The IRAS Moving Source and Cometary Dust Trail Survey

In a systematic examination of 1836 band 1, 2, 3, and occasionally band 4, Sky Brightness Images, 466 sources (Fig. 7) that are thought to be Earth orbiting satellites, were discovered. During the survey one new cometary dust trail, associated with the periodic comet Pons-Winnecke, was also found (Dow and Sykes 1988, Sykes and Walker 1992)

The IRAS Sky Brightness Images and the CRDD are the primary sources of information about the Earth orbiting objects found in this survey. The Sky Brightness Images were used to find the Earth orbiting objects and their positions. Using these positions, more detailed information was obtained from examining the CRDD. A complete set of Sky Brightness Images is located at Steward Observatory; however, the only US depository for the CRDD is IPAC.

The Sky Brightness Images were constructed from scans of the sky acquired during a given HCON. The Images are divided into 212 fields that are located on 15° centers and have 2 arc-minute pixels that have a resolution of four to six arc-minutes. The Sky Brightness Images are actually 16.5° on a side to allow for some overlap. The sky was mapped in each of the four IRAS passbands. In constructing the Sky Brightness Images the detector outputs were "phased" so that the flux from a fixed source, which was observed by different detectors, would map onto the same location. In a single passband Image, a moving source appeared to be two point sources very close together— corresponding to the two focal plane detector modules. As seen in Figure 2, however, the

image of a moving source was extended when more than one Sky Brightness Image from different passbands in the same field were superposed. The CRDD contains a record of the date and Universal Time of all observations. The angular motion, the observed flux from a source and the average sky background registered in each detector, as a function of the sampling rate, can also be determined from the CRDD.

Fifty-four sources, forty-five of which are best described as objects in Earth orbit (Table 2), were selected from the original sample to determine their orbital and thermal characteristics. The other nine objects are asteroids, flashes from the internal reference source or possibly cosmic rays. The sources are characterized by (1) their extent across a Sky Brightness Image when three bands are overlaid (as far as 40 arc-minutes in some cases), (2) their apparent brightness on an Image and (3) their orientation along the in-scan direction. The fifty-four sources were chosen so that at least one object representing each of these three different types that were seen on the Sky Brightness Images. Several sources that appeared unusual, as well as a few examples where two sources appeared close together on an Image, were also selected. Scientifically, a random approach to selecting the sources may have been equally, if not more, appropriate. The impetus for the appoach used in this study, however, was to sample as many different types of sources as possible. The number of objects that could be examined was limited by the large amount of interactive computer time required to extract the CRDD using the IPAC magnetic tape archives.

Distribution on the Sky of Objects Discovered During the IRAS Moving Source and Cometary Dust Trail Survey
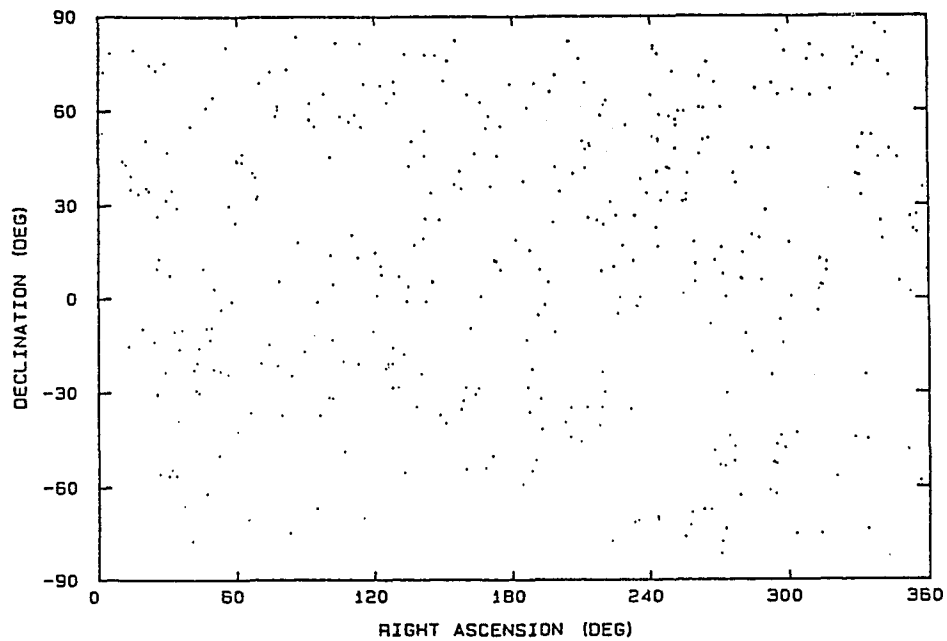
Figure 7: The distribution of 454 sources discovered on the IRAS Sky Brightness Images. The 12 near-field sources discussed in Chapter One are not plotted. On an equal-area projection, a concentration of objects towards the the north celestial pole would be obvious.

TABLE 2
Flux Density and Angular Motion of Earth Orbiting Sources

source #	B1 (A)	B1 (B)	B2 (A)	B2 (B)	B3 (A)	B3 (B)	B4 (A)	B4 (B)	ang mot	1/2 CC Temp
15	21.48	21.45	42.20	80.39	27.19	21.33	9.94		99.00	229.00
18	90.74	94.46	113.64	111.10	152.27	305.23	347.26	433.44	72.00	358.00
47	793.32	388.15	1056.10	1066.54	207.47	419.03		205.56	6.12	331.00
48	107.18	45.41	83.89		29.34	44.47	313.90	132.93	270.03	465.00
49	18.89	19.64	19.08	35.47					214.00	284.00
74	48.22	29.61	44.15	32.29	39.92	20.50			71.00	389.00
75	17.66	31.08	13.38	2.37	30.71	19.75			1.29	797.00
94	52.54	112.78	203.27	109.99		83.99	28.27		42.33	285.00
95	48.10	49.29	49.66		25.74	19.71	10.13	19.71	71.00	348.00
102	103.56	108.89	75.60	60.20	13.09	12.24			3.44	505.00
102	17.15	42.45	29.77	40.51	17.60	22.76			90.00	398.00
104	125.40	132.35	103.09		207.57	249.74	186.79		76.00	466.00
109	121.34	155.63	133.30	155.98	211.58	467.75	264.09		68.00	388.00
133	58.53	54.05	119.03	137.19	442.66	197.14			87.00	252.00
163	21.12	19.72	31.75	18.56					121.00	312.00
176	185.44	376.64	14.66	274.97	287.44	20.72	357.07	229.33	42.50	473.00
177	176.63	34.89	196.47	226.22	47.51	63.66	469.49	193.44	139.00	339.00
193	129.76	104.32	170.16	169.63	68.51	53.44			16.52	332.00
194	15.81	15.25	7.78	7.95					4.57	464.00
214	69.70	90.13	79.44			273.98	144.12	174.74	63.00	475.00
215	35.33	44.35	34.77	38.76	14.59	29.44	11.61	10.54	104.96	442.00
228	217.66		307.09			126.47			5.27	323.00
230	11.70	12.15	20.43	21.01	9.72	8.50			8.19	290.00
231	16.69	66.44	65.53			16.50			25.54	392.00
250	44.43	53.71	52.16		225.96	225.01			81.00	393.00
251	55.74	59.37	80.12	58.89	11.70	21.71	38.43	16.10	16.40	330.00
252	69.63	70.16	103.24	85.26	40.19	42.16			9.01	316.00
253	167.20	114.70	175.14	145.66	48.55	51.44			14.12	378.00
274	36.13	44.95	55.58	58.37	7.18	15.97			67.60	345.00
280	14.68	10.46	18.72	17.21	11.46	12.30			27.57	340.00
281	14.30	9.93	25.51			7.45			4.83	287.00
282	12.37	12.20	17.20	14.87	5.15	4.99			5.26	325.00
305	5.73	6.98	10.76	13.58	3.48	3.94			4.46	274.00
333	303.45	135.80	58.47	504.48	152.69	114.63			9.05	350.00
345	123.42	145.78	141.31	111.20	103.52	178.31	248.78		41.00	394.00
368	32.35	36.63	8.40	23.94	34.36	19.57	73.68	18.05	80.75	534.00
369	26.91	25.13	39.27	36.78	6.83	16.14			5.73	317.00
371				102.76		44.69			16.90	
372	31.57	10.02	17.50	46.89	14.75	10.52			4.87	318.00
373	7.56	7.76	14.51	13.68	7.17	6.95			5.30	280.00
375	73.27	136.59	34.00		133.05		30.04	65.46	41.00	741.00
376	43.49	78.19	48.95	19.72	175.79	232.53			121.04	564.00
415	14.33	21.26	27.61		7.11	8.19			31.60	337.00
453	353.68	404.59	168.30	86.78		106.99	130.09		46.44	237.00
454	27.59	18.47	17.02	21.03	4.00	3.40			3.89	474.00

column 1 = source number
column 2 - 9 = module A and B flux density in band 1 (B1) through band 4 (B4) quoted in Janskys
column 10 = angular motion of source as seen from IRAS in arc-minutes/second
column 11 = band 1/band2 color corrected temperature in degrees Kelvin

The first step in the search procedure was to superpose and display the HCON 1 Sky Brightness Images from band 1, 2 and 3 on an image processing system. Similarly, HCON 2, and when available HCON 3, Images were displayed in separate frames. These frames were then "blinked" against one another to find sources that either showed movement or completely disappeared. To facilitate finding debris, payloads, comets, asteroids, astronomical sources that might have been missed during the compilation of the Point Source Catalog, or anything that appeared unusual, an existing program (developed by the Infrared Group at Steward Observatory) that placed a small cursor over any source that was listed in the Small Scale Structure Catalog or the Point Source Catalog, was used when examining each image.

The right ascension and declination of an object were determined directly from the Sky Brightness Image by using a screen management routine developed at IPAC. This routine involved placing a cursor over a desired location on the Image with a trackball and then writing the coordinates to an output file. Given the position of a source, the IRAS CRDD that corresponded to the observation could be obtained. When examined closely, however, the moving sources appeared to have a jagged shape on the Sky Brightness Images simply because the pixels are square in shape. This made defining the exact center of an object a matter of visual judgment. While the position may have been in error by one or two pixels, it was not significant enough to make finding the CRDD a problem. Typically, the image of a piece of debris or a payload covered six to eight pixels when band 1, 2 and 3 Sky Brightness Images were overlaid.

The second step in the project was to examine the IRAS CRDD for all fifty-four sources. Two visits were made to IPAC to obtain the CRDD. Since it was known in which of the three HCON's the Earth orbiting object appeared, the full focal plane detector outputs for

no more than three SOP/OBS had to be examined. Still, this represents 62 x 3 or 186 CRDD strip charts for every source! The most efficient way to examine the CRDD was interactively on a computer terminal. Forty seconds of data, centered on the time of observation, were viewed for each detector. A moving source in one set of SOP/OBS was distinguished by spike-like profiles in the CRDD strip charts near the specified Universal Time. The CRDD from the other candidate SOP/OBS showed only background noise. After the correct SOP/OBS was located, the CRDD strip charts were separated according to passband making it easier to identify the detectors which observed the source. The path of the source in front of the focal plane was defined by the strongest signals in each passband. In all cases, the flux from a moving source was registered by two or three detectors in each passband.

2. Characteristics of Earth Orbiting Objects Observed by IRAS

The methods employed in this study to determine the angular motion, flux density, temperature and inclination of the 45 Earth orbiting objects, are outlined in the following sections. A catalog that contains the passband, position and HCON for all 466 objects can be found in the Appendix 1 of this document.

2.1. Angular Motion and Altitude Predictions

To determine the approximate angular rate of the Earth orbiting objects found in this survey, the distance between two detectors over which the source passed was divided by the time difference between the peak fluxes in the corresponding detectors (Fig. 8). The timing information and the specific detectors that registered the maximum flux are found in the CRDD. The CRDD used for this project was not "time-shifted" to account for the

IRAS scan rate. The distance between detectors is listed in the IRAS Explanatory Supplement (IRAS Catalogs and Atlases 1988). Generally, information from the 12 and 25 μm passband detectors was used to determine angular motions, although, for sources moving in front of the focal plane in the y-direction, any two detectors in any passband could have been used. This is because the sampling rate was directly proportional to the detector width. The dimensions of all the detectors, however, are roughly the same in the z-direction. For sources passing in front of the focal plane in a direction offset from the scan direction (Fig. 9), the band 1 and band 2 detectors had to be used because they had the highest sampling frequency.

Point sources always passed in front of the focal plane and in the image direction with an apparent angular motion equal to the IRAS scan rate—3.85 arc-minutes/second. Since the focal plane was 46 arc-minutes in diameter in the y-direction, a point source crossed the focal plane in 11.95 seconds. This means that a point source was always sampled three times on a detector. The sampling frequency ν_s is determined by calculating the dwell time T_d on a detector and then dividing by the sampling rate t_s :

$$\nu_s = T_d/t_s$$

By definition: $T_d = x/\omega$
where: x = detector width
ω = angular motion

For the 12 and 25 μm detectors:

$$T_d = x/\omega = 0.76 \text{ arc-minutes}/(3.85 \text{ arc-minutes/second}) = 0.19 \text{ seconds}$$

$$\therefore \nu_s = T_d/t_s = 0.19 \text{ seconds} /0.0625 \text{ seconds} = 3.04$$
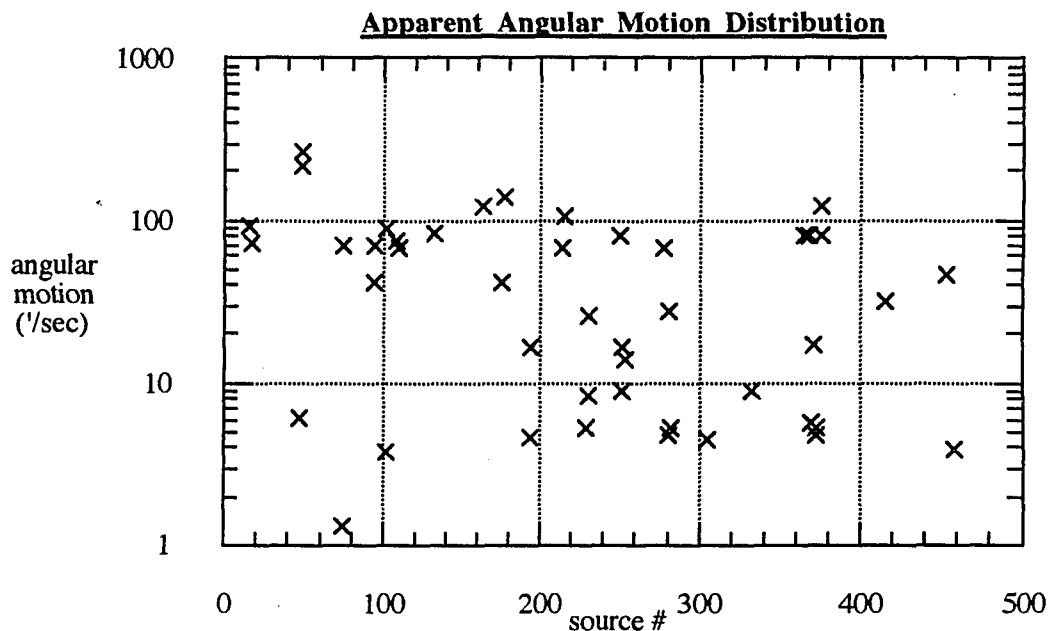
Figure 8. There are 20 sources with angular motions less than 25 arc-minutes/second that may be artificial satellites tracked by the USSPACECOM. The remaining 25 sources may be small pieces of untracked debris close to the IRAS focal plane. Of the nine sources that are not plotted, three were found to be cosmic ray events, three were flashes associated with the internal reference source and three were asteroids. Cosmic ray events have very high angular motions and illuminate one or a few detectors simultaneously. The internal reference sources were flashed at the beginning and end of each survey scan to monitor the responsivity of the system. It is unclear why these flashes are seen on the Sky Brightness Images and why they have the same appearance as the Earth orbiting sources. (Two sources, 109 and 214, both have an angular motion of 68.0 arc-minutes/second.)

Dimensions of a 12 μm Detector Indicating the Maximum Distance in Front of the Focal Plane that an Object Can Travel
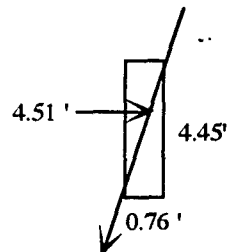
Figure 9: For sources moving in front of the focal plane at an angle, the distance across the detector will be no more than 4.51 arc-minutes for the 12 μm detectors. (See the dwell time calculation outlined in the text.) With regard to the detection of orbital debris, large detectors with high sampling frequencies are desirable for reliable fluxes, particularly for fast moving sources.

IRAS Detector Dwell Time
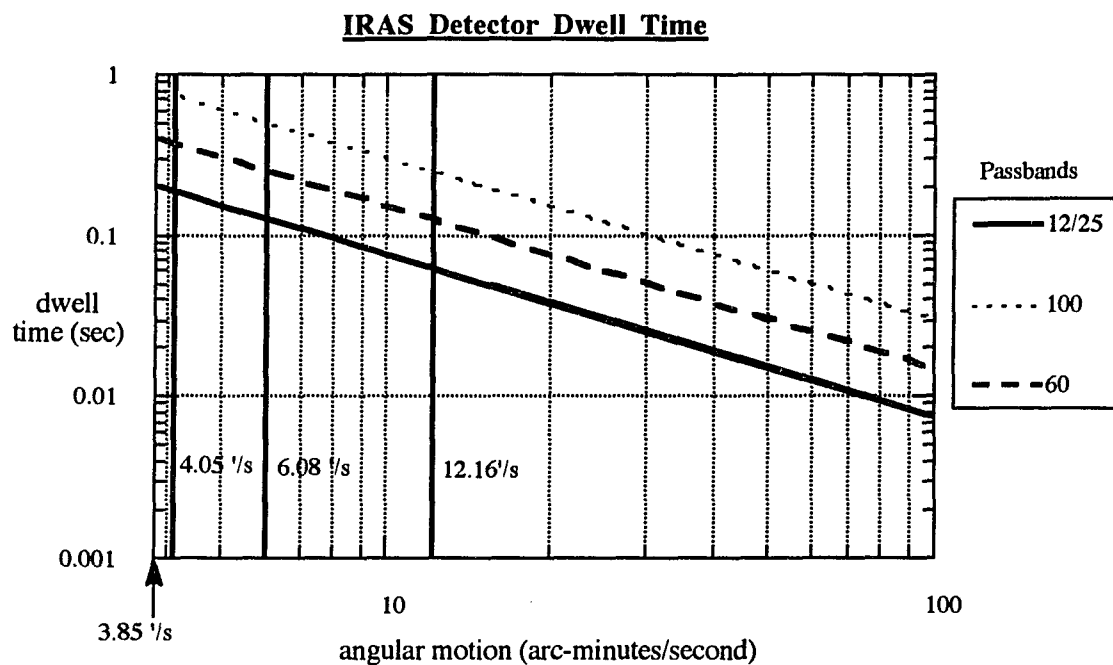
Figure 10: IRAS detector dwell times for sources moving in front of the focal plane in the y-direction. A source moving with an angular motion of 4.05 arc-minutes/second has a sampling frequency of three; whereas, a source moving at 6.08 arc-minutes/second has a sampling frequency of two and a source moving equal to or greater than 12.16 arc-minutes/second had a sampling frequency of one.

This simple calculation has some important implications for moving sources. Any moving source which crossed the focal plane in the y-direction in 3.78 seconds or less (an angular motion equal to or faster than 12.16 arc-minutes/second) was sampled a maximum of one time on a detector. This means that sources moving slower than 12.16 arc-minutes/second should have the most reliable fluxes and the most accurate temperatures (Fig. 10). While objects moving equal to or faster than this rate may have been fully sampled, it is equally likely that they were only partially sampled on the edge of a detector. Only nine sources were found that could have been sampled three times and four were found that could have been sampled twice. The remaining 31 sources were sampled no more than once. These sources are probably very close to the focal plane given their very high angular motions. The method used to determine accurate fluxes in view of this problem is discussed in the next section.

There are two sources of error associated with calculating the angular motion of an Earth orbiting source observed by IRAS. The first source of error results from trying to locate where on the detector most of the flux was sampled. The second possible error is in knowing the exact time that the peak flux was sampled. Clearly, the two errors are related. For example, a source that passed between detectors 51 and 23, which are separated by 16.89 arc-minutes, in 3.38 seconds would have an approximate angular motion of five arc-minutes/second. If the actual time is in error by ± 0.125 seconds (two times the sampling rate) the angular motion will be in error by ± 0.2 arc-minutes/second. This is the largest angular motion error that is expected because moving sources were never sampled more than three times. For the more slowly moving sources the error should be less than this. Given this small error and the high angular motions of the majority of the sources, a more precise error analysis is unnecessary.

With one exception, all 45 debris particles and artificial satellites pass in front of the focal plane in the image direction. In other words, the objects are moving in the same direction that iRAS is scanning. Half of these objects were found to be in orbits inclined to the scan direction and the other half, although they did not always pass though the boresight of the telescope, were not offset from the y-axis of the focal plane. The objects that are moving along the scan direction must be in orbits that are similarly inclined to IRAS. The fact that there are so many sources that behave in this manner is not surprising, given the population of objects in highly inclined orbits (Fig. 11).

Using the value of the angular motion (n'), as measured on the CRDD, the altitude of a source passing in front of the focal plane and *moving in nearly the same plane and the same direction around the Earth as IRAS* can be determined (Fig. 12) according to the following formula:

$$n' = (n_{scan} - n_{iras}) - (n-n_{iras}) [R/(R-r)]$$

where n_{scan} is the IRAS scan rate (3.85 arc-minutes/second), n_{iras} is the angular motion of IRAS as seen from the center of the Earth (3.5 arc-minutes/second), $n = (GM/R^3)^{1/2}$ is the true angular motion of the object as seen from the center of the Earth, r is the distance of IRAS from the center of the Earth and R is the distance between the source and the center of the Earth. The gravitational constant is G and M is the mass of the Earth. This formula, derived in Appendix 4, is general for debris in circular orbits. This is a valid approximation because atmospheric drag and solar radiation pressure tend to circularize the orbits of debris particles.

1983 Inclination Distribution

Objects Tracked by the USSPACECOM Above 900 kilometers
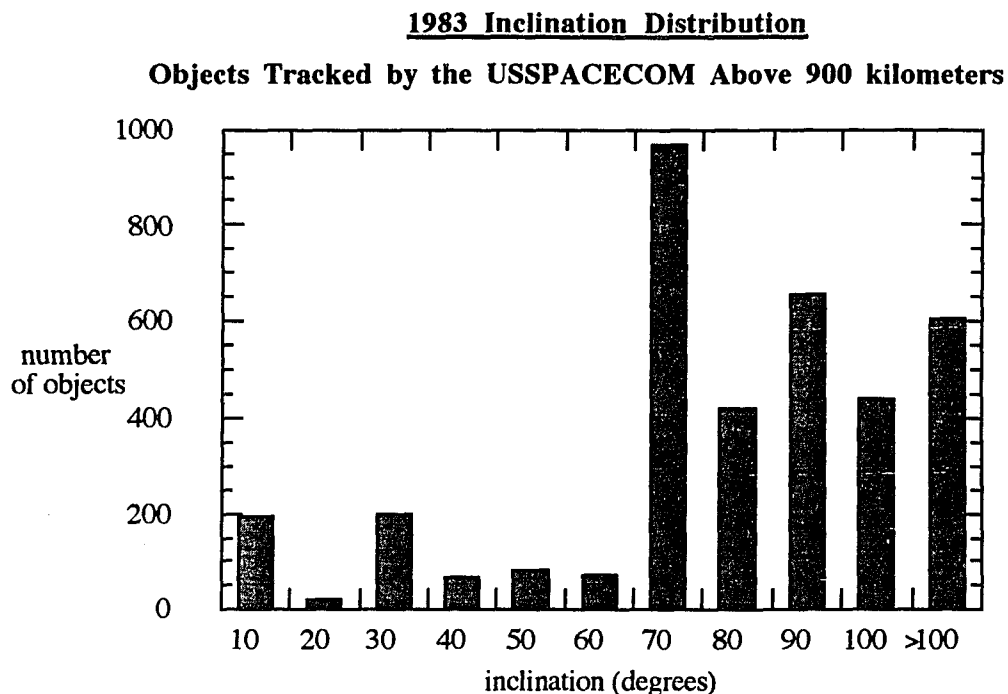
Figure 11: There were 3570 objects in orbit at altitudes higher than 900 km in 1983. Almost all of these objects were in near circular orbits: 48% had eccentricities less than or equal to 0.01 and only 9.9 % had eccentricities greater than 0.5. Although the distribution of debris with inclination is essentially uniform at altitudes below 1000 kilometers, most payloads and debris fragments above this altitude are distributed at inclinations near 75°, 63° (Plesetsk launches), 82°, 100° (Sun-synchronous orbits), >100°(debris from fragmentations in Sun-synchronous orbits), 90° (polar orbits) 28.5° (Kennedy Space Center launches) and 0°(Geostationary orbits).

Apparent Rate of Artificial Satellite Motion in Front of the IRAS Focal Plane
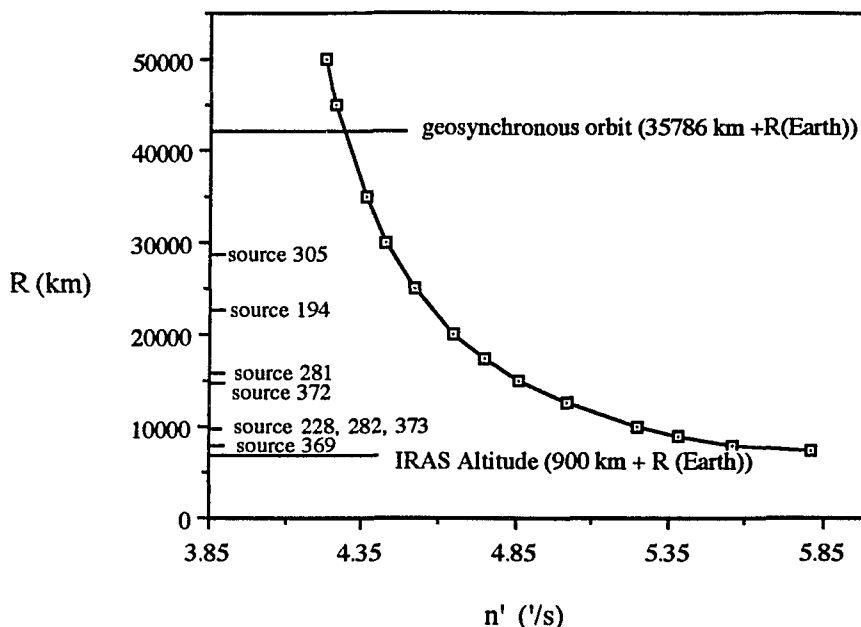
Figure 12: The angular motion (n') and corresponding altitude for artificial satellites moving in circular orbits around the Earth and in a similar orbital plane to IRAS. R is the distance to the satellite from the center of the Earth and n' = $(n_{scan} - n_{iras}) - (n-n_{iras}) [R/(R-r)]$. As R approaches infinity, n' will approach 3.85 arc-minutes/second. The sources indicated on the graph are at the following predicted altitudes for circular orbits as calculated from the above formula: Source 369 (7525 km), Source 373 (9550 km), Source 228 (9800 km), Source 282 (9900 km), source 372 (14900 km), Source 281 (15700 km), Source 194 (23000 km) and Source 305 (28000 km). The angular motion of each source used in this calculation is listed in Table 2. Sources 373, 282, 228 and 305 were correlated with known artificial satellites. Of these four objects, only Source 228 was in a near circular non-geosynchronous orbit. The angular motion of Source 228 was 5.27 arc-minutes/second. If an error of ± 1 arc-minute/second is assumed, the predicted distance range for this object is between 10,700 kilometers and 9000 kilometers. Source 228 was correlated with the payload FTV-ERS 10 at an altitude of 10,178. Source 373 and Source 282 were in highly eccentric orbits and Source 305 was a geosynchronous satellite. Geosynchronous satellites have a non-uniform apparent motion, which is a function of the inclination and the eccentricity of the orbit, as seen from IRAS or from the surface of the Earth. This type of satellite circles the Earth in 1436 minutes, equalling the Earth's sidereal rotation period relative to the celestial background. Geosynchronous satellites that are in equatorial orbits are called geostationary satellites. There are about 300 geostationary satellites in Earth orbit. Satellites with very high angular motions are likely to be small pieces of debris, such as paint flakes, directly in front of the focal plane.

For objects that are very close to the focal plane this formula will break down. A more sophisticated calculation would take eccentric orbits and various inclinations in to account, although some knowledge of where the object was observed in its orbit would be required.

2.2. Flux Density and Temperature

Before accurate temperatures for the 45 Earth orbiting objects could be calculated, reliable flux densities had to be determined for every source. While the flux density of astronomical sources can be estimated using the cursor routine described in section one of this chapter, it is not a reliable method for moving sources. This is because a moving source appears in one SOP/OBS and the Sky Brightness Images are *averages* of several scans from two or three SOP/OBS. The flux density of a moving source can only be determined from the CRDD.

The analog-to-digital units (ADUs) listed in the CRDD were converted to flux densities using the following formula:

$$\frac{(\xi)\,(BCF)}{(\Delta\lambda)}\,(10^{-26}) = F$$

ξ = number of ADUs
BCF = band conversion factor (Watt m^{-2})
$\Delta\lambda$ = bandwidth (Hz)
F = flux density (Janskys)

where: 10^{-26} Watt m^{-2} Hz^{-1} = 1 Jansky

The BCF, which takes the detector sensitivity into account, was set at the beginning of each scan by the flux calibrator, "internal reference source", described in Chapter One.

Source 373 Gaussian Fit to Flux Density

WAVELENGTH BANDS, μm

Path of Source 373

IMAGE
DIRECTION

VISIBLE
STAR
SENSORS
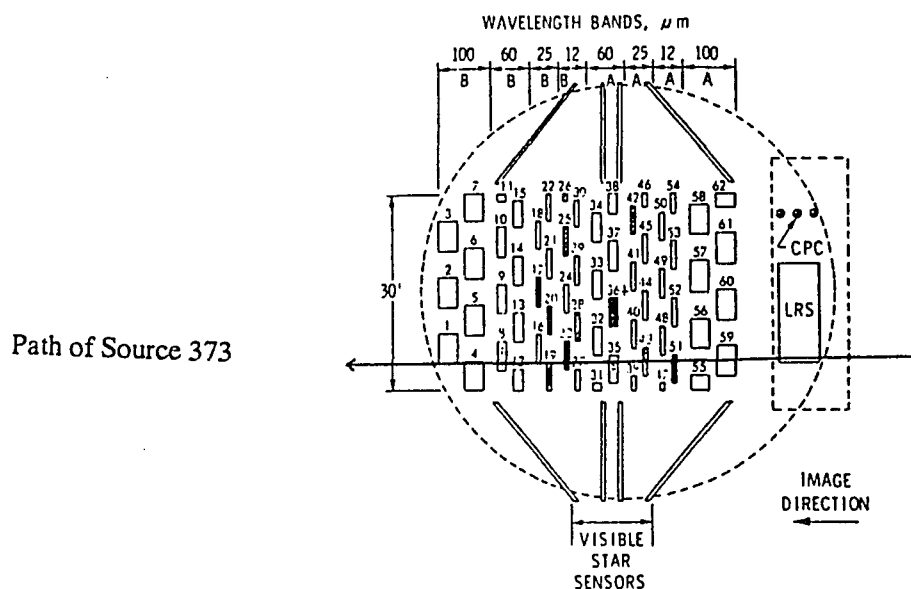
Figure 13a: Source 373 passed over the lower portion of the IRAS focal plane. This object is the final stage of the Soviet SL-6 rocket that launched Kosmos 1409, an early warning payload, on 22 September 1982. Source 373 had an angular motion of 5.3 arc-minutes/second and a color corrected temperature of 280 K.

Source 373 Gaussian Fit to Flux Density
Band 1
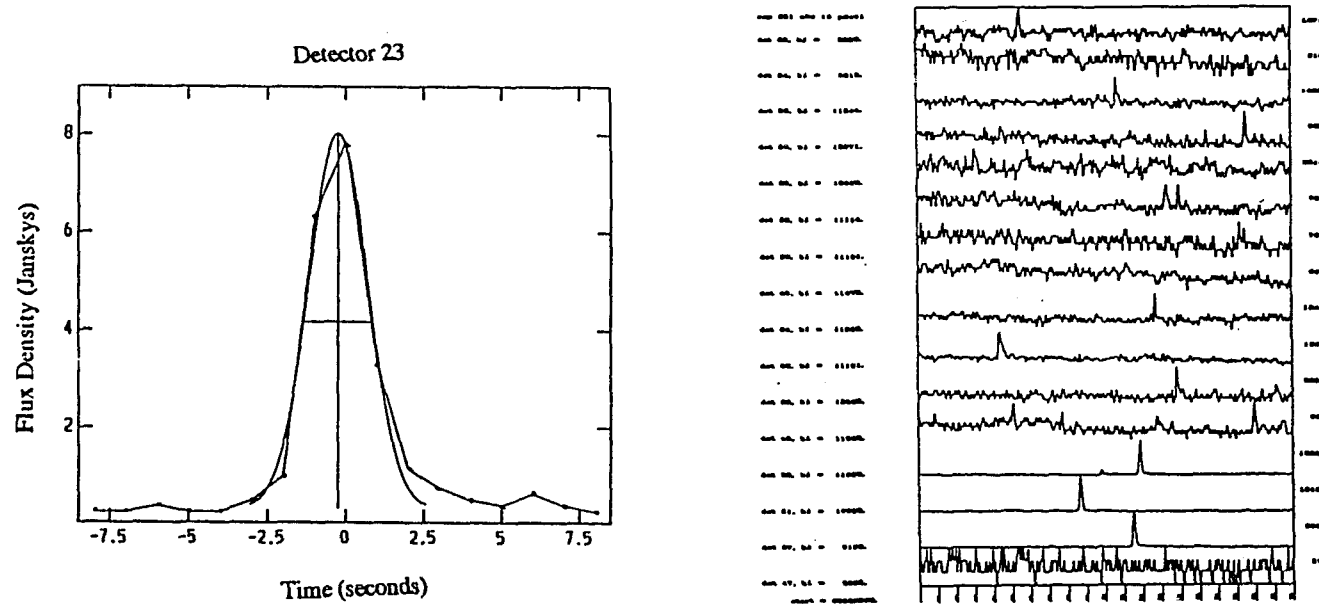
Detector 23

Figure 13b: On the right hand side is 20 seconds of band 1 CRDD from SOP 351 OBS 18. Source 373 passed over three detectors: 23, 51 and 27. The flux was strongest in detectors 23 and 51. The scale on the bottom of the CRDD strip chart is one second intervals of Universal Time. The scale along the right hand side is the flux of the source above the background in units of $10e-16$ W m^{-2}. The left hand side list the band and detector number followed by the background level in the same units. At the bottom left corner of the chart is the UTCS start time for this piece of CRDD. At the top on the left is the SOP/OBS designator. On the left hand side of the figure is the profile from detector 23. One second, or sixteen samples, are plotted. The points indicate when the flux from the source was sampled. The flux density as determined from detector 23 was 7.76 Janskys.

Source 373 Gaussian Fit to Flux Density
Band 2
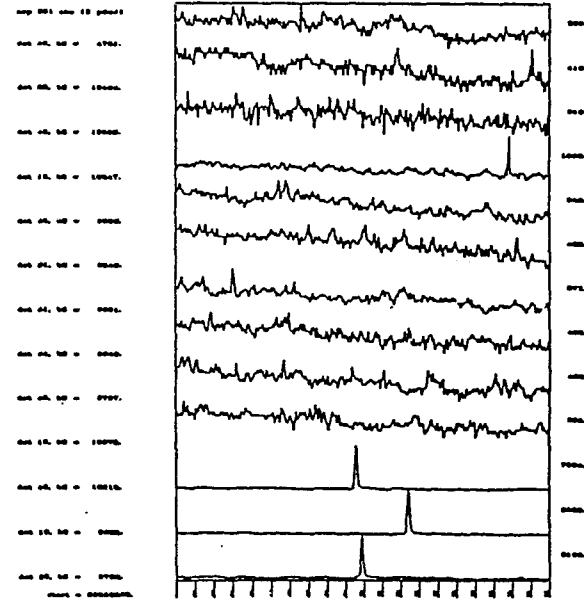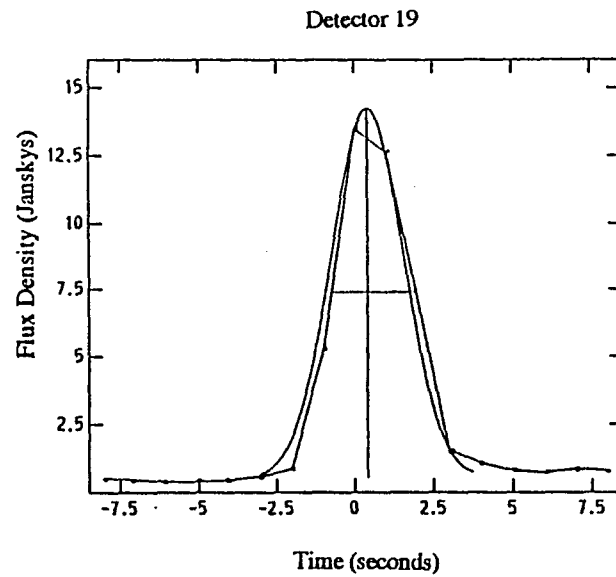
Detector 19

Figure 13c: On the right is band 2 CRDD for Source 373. The source passed over detectors 19 (13.68 Jy) and 43 (14.51). One second of data has been plotted on the left for detector 19.

44

Source 373 Gaussian Fit to Flux Density
Band 3
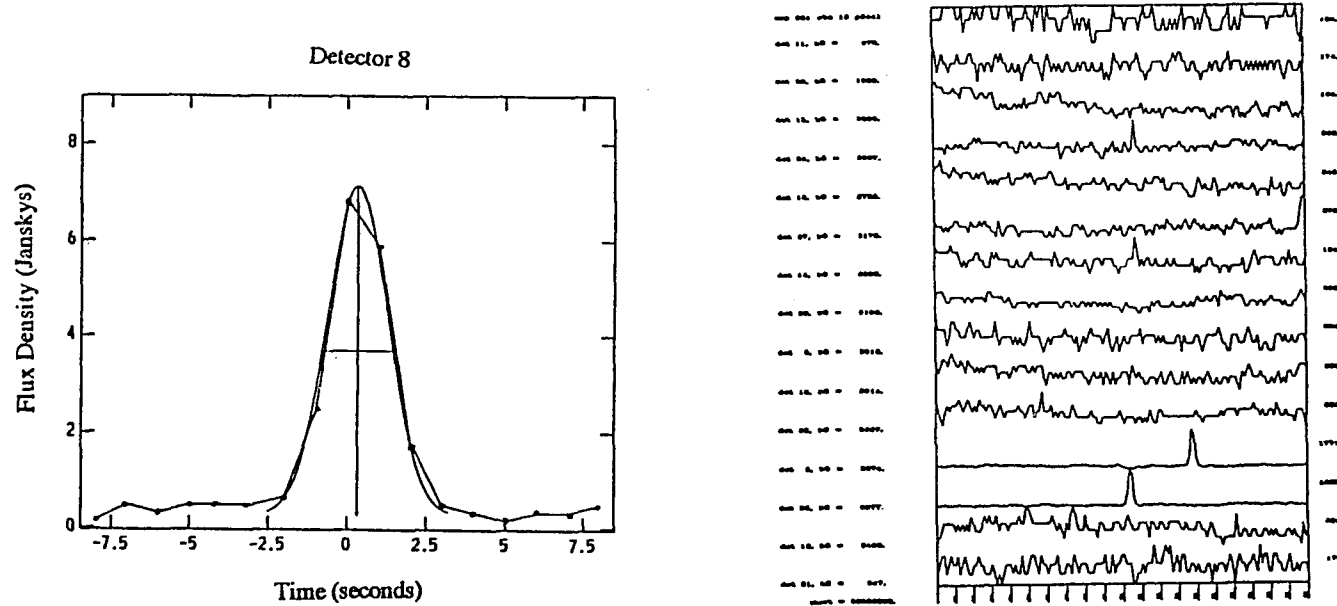
Figure 13d: The CRDD for Source 373 band 3 is on the right. The source passed closest to detectors 35 (7.17 Jy) and 8 (6.93 Jy). Sixteen samples, which is 2 seconds of data, for detector 8 has been plotted and fit with a Gaussian profile on the left.

Although the sampling rate was high, it was obvious from examination of the source profiles in the CRDD strip charts that, in numerous cases, the flux was not fully sampled on the center of the detector (Fig 13 a-d). To get a better estimate of the true flux density in each passband, therefore, the profiles from each detector that the object passed over were replotted and then fit with a Gaussian. One second of data for band 1 and band 2 and two seconds of data for band 3, which corresponded to 16 samples of the flux for every source, were plotted. A more sophisticated fitting routine was not required due to the quality of the data. Typically, at least one detector in each passband pair sampled the flux near the center of the detector,although for some sources the flux from the object was never fully sampled in any detector. The Gaussian routine proved effective in getting a better estimate of the peak flux in each passband. For example, there were 43 sources that had data in each band 1 module. In 86% of the cases, the higher flux agreed to within 50% of the flux in the other module and for 54% of the cases, this agreement was to within 25% of the flux in the other module. In band 2, there were 34 sources where a detection was made in both modules. Of the higher of the two fluxes, 85% agreed to within 50% of the lower flux, while 59% of the higher fluxes agreed to within 25% of the lower of the two values. The average sky background, over the time interval specified, was provided when the CRDD strip charts were generated. These values were subtracted before the Gaussian fitting of the flux profiles.

By multiplying a blackbody spectrum with the spectral response of the IRAS detectors, the color temperature of the sources in the survey can be calculated—given the ratio of the observed flux densities in two bands. The spectral response values of the IRAS passbands can be found in the IRAS Explanatory Supplement (IRAS Catalogs and Atlases 1988). Alternatively, color correction factors, listed in the Explanatory Supplement, can be used to determine the color temperature of objects observed by IRAS. The temperature must be

color corrected because the flux may be non-linear across the bandpass. A partial listing of the color correction factors from the Explanatory Supplement is found in Table 3.

In this study, the higher of the two band 1 fluxes and the higher of the band 2 fluxes were used to determine the 12/25 µm color temperature. To calculate the color corrected temperature of an object using the Color Correction Tables:

1. Determine the IRAS observed flux ratio $J = F1/F2$
2. Find the nearest entry in the Aumann color correction table for J. Use linear interpolation if an exact match is not found.
3. Multiply J by C2 and divide by C1. This is the band 1/band 2 color corrected flux.
4. Find the new ratio in the Aumann table and read the value of the color temperature in the left hand column.

where:
J = band 1/band 2 IRAS observed flux flux
F1 = band 1 IRAS observed flux
F2 = band 2 IRAS observed flux
C1 = band 1 color correction factor
C2 = band 2 color correction factor

The 12/25 µm color temperatures of the 45 Earth orbiting objects are plotted in Fig. 14. In almost every case, the 12/25 µm color corrected temperatures were significantly different from the 25/60 µm color corrected temperature—sometimes by as much as 50%. This may be because the band 1 and band 2 detections were de-glitched by a different amount when compared to the band 3 detections. This error is difficult to trace as it is impossible to say when the de-glitcher was triggered. More likely, the temperature discrepancy is due to the fact that most of the flux from a 300 K blackbody falls in band 1, where the spectral response is 46%, and band 2, where the response is 50%. In band 3 and band 4, which is the Rayleigh-Jeans portion of the spectrum for a 300 K blackbody, the spectral response is much lower, 36% and 17% respectively. The color temperature determined from the

Temperature	C1	C2	F1/F2
400	1.01	1.22	1.272
300	0.92	1.15	0.785
290	0.91	1.15	0.734
280	0.90	1.14	0.684
270	0.89	1.13	0.633
260	0.88	1.12	0.583
250	0.87	1.11	0.534
240	0.86	1.09	0.486
230	0.85	1.08	0.438
220	0.85	1.07	0.392

TABLE 3
COLOR CORRECTION FACTORS*

*(IRAS Catalogs and Atlases 1988).

12/25 Micron Color Temperature Distribution
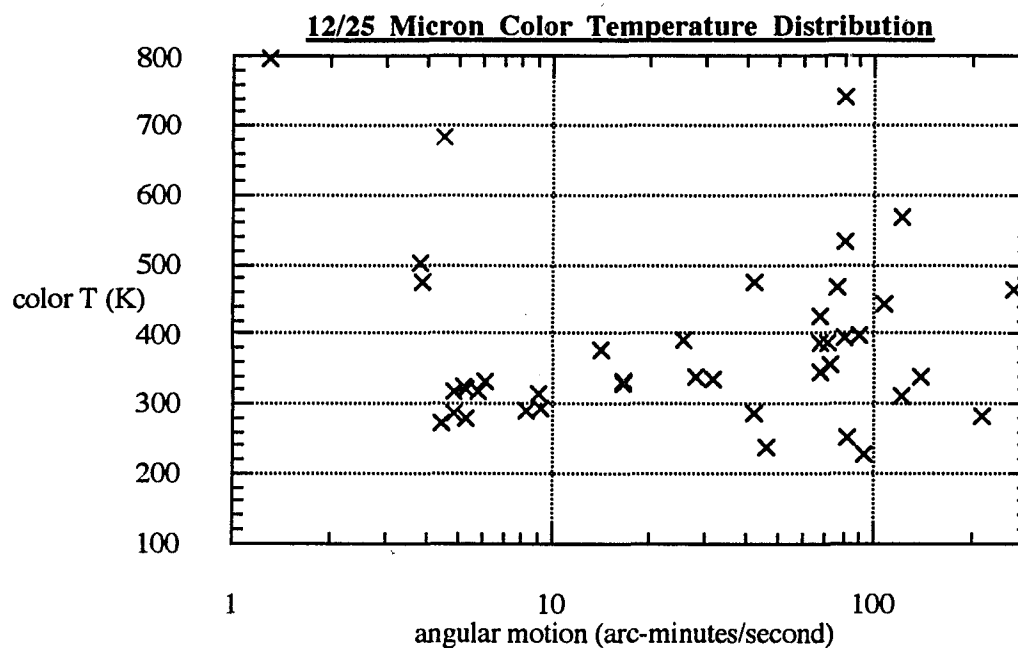
Figure 14: The color corrected temperatures for 45 Earth orbiting sources observed by IRAS. It should be noted that due to the orientation of IRAS relative to the Sun, many objects were observed near a phase angle of 90° and will therefore be at their hottest or their coolest temperature when they were detected (Lebofsky and Vilas 1990). This may contribute to the wide range of 12/25 μm color temperatures observed.

Rayleigh-Jeans tail is less accurate than the color temperature determined from points near the peak of the blackbody curve. Yet another possible explanation for the different color temperatures is that this analysis treats Earth-orbiting objects as blackbodies, when technically they are graybodies whose emissivity may change as a function of wavelength.

The temperature of a piece of debris is a function of its orientation with respect to incoming sources of radiation, the amount of time that it was illuminated, its geometry, its rate of rotation and the material of which it was constructed. The purpose of the thermal control surfaces on a payload, operational or not, is to keep a satellite from having significant swings in temperature as it passes in and out of the Earth's shadow. Debris fragments, on the other hand, have no means by which to regulate their temperature.

It can be seen in Fig. 14 that many of the slower moving sources in this study have temperatures near 300 K, which is roughly the average temperature that is expected for an object at the Earth-Sun distance. Temperature is correlated with angular motion because the slower moving sources are expected to be intact satellites which are in well defined orbits. The faster moving sources are more likley to be debris. Objects which are not intact are more likely to be subject to greater temperature swings as the object passes in and out of the Earth's shadow. The sources with low angular motions and high temperatures may be pieces of debris such as a rocket body made from aluminum, which has a very high calculated equilibrium temperature. It is also possible that, for whatever reason,these particular objects have poorly determined fluxes because the source was not fully sampled on the IRAS detectors—leading to a poorly determined temperature. The sources with angular motions greater than 10 arc-minutes/second cover a range of temperatures because of the many different types of materials that make up the debris population. In short,

temperature implies composition regardless of angular motion. Spacecraft materials are discussed in greater detail in Chapter Three.

3. Moving Astronomical Sources

Many moving astronomical sources were also observed by IRAS, particularly asteroids, which are bright infrared sources at 12 and 25 μm. During the mission, 1811 known asteroids were detected (IRAS Catalogs and Atlases 1988) and two new Apollo and two new main belt asteroids were discovered. Six new comets were also found (Walker *et al.* 1986).

3.1 Asteroids

The properties of 1811 asteroids (7015 sightings) with known orbits and 25 comets were determined as part of the IRAS Asteroid and Comet Survey. Asteroid diameters and albedos were calculated using a form of the "standard" thermal model based on ground based observations of Ceres and Pallas (Lebofsky 1986). Standard thermal models of asteroids have been extended to characterize IRAS observations of orbital debris (Lebofsky and Vilas 1990).

Three asteroids, 36 Atalante, 694 Ekard and 276 Adelheid were found and cataloged during the visual examination of the Sky Brightness Images part of this study because they were both bright and were not in the Point Source Catalog. The asteroids were correlated using computer software available from IPAC. It was not known during the survey that they were asteroids. It can be anticipated that there are several other asteroids in the main sample. The color corrected temperature of 36 Atalante varied between 242 K and 246 K

over a fourteen hour period; the color corrected temperature of 694 Ekard varied between 248 K and 262 K over a ten hour period and 276 Adelheid, which was sighted only once, had a temperature of 230 K. The asteroids 36 Atalante and 694 Ekhard were seen during three different orbits and 276 Adelheid was seen on one orbit on the day indicated in Table 4.

3.2 Pons-Winnecke Dust Trail

Dust trails are millimeter and larger sized particles that are ejected by some short period comets during perihelion passage into orbits near the parent comet. The particles are in orbits nearly identical to the comet and extend both ahead and behind its orbital position. Seven cometary dust trails, associated with short-period comets, were identified (Sykes *et al.* 1986) before this study. One new cometary dust trail, associated with the comet Pons-Winnecke, (Table 5) was discovered during this survey (Dow and Sykes 1988). Some of the trails extend several to tens of degrees in apparent length across the Sky Brightness Images.

Summary of Chapter Two

Artificial satellites and debris can be found on 160 of the 212 Sky Brightness Image fields covering the sky. Six or more sources can be found on twenty of the Images. Image number 209 is the most contaminated, with thirteen sources in the 16.5° square field. As demonstrated by the analysis described in this paper, however, some of these source are in fact asteroids. It is anticipated that more moving sources will be revealed when the de-striped Super Skyflux Images are released by IPAC. Of the 45 sources studied, 66% have

angular motions greater than 10 arc-minutes/second and must be near the focal plane. The corrected color temperature of 76% of the objects was between 200 and 400 K.

In Chapter Three, the basic thermal behavior of artificial satellites and debris in earth orbit and the characteristics of the orbital debris population are described. It is critical to evaluate these factors during the mission planning phase of any space-based operation. Astronomical satellites using optical and infrared detection systems are particularly susceptible to interference from Earth orbiting objects. The results from this study, which complement and contradict what we know about the debris population, are also highlighted in the next chapter.

TABLE 4

Characteristics of the Asteroids Atalante, Ekard and Adelheid

Asteroid	Date Obs. on SBI*	RA	Dec	Diameter (km)	Phase Angle (deg)	Distance (AU)
36 Atalante	11 Oct.	6:42:31	+45:11:44	109	30.56	2.75
694 Ekard	7 July	23:40:00	+21:04:10	92.7	33.39	2.67
276 Adelheid	5 Nov.	20:51:31	+02:64:54	122	17.42	3.12

*Sky Brightness Image

(Asteroid characteristics are from Tedesco 1989)

TABLE 5
Pons-Winnecke Cometary Dust Trail Positions in the
Band 1, 2 and 3 Sky Brightness Images

Image Number	HCON			RA and Dec Position		
120	1	01:04:45	-18:05:35	to	00:39:21	-20:30:20
120	2	01:32:11	-19:06:57	to	00:59:08	-22:51:01

CHAPTER THREE
Space-Based Observations of Orbital Debris

1. Orbital Debris Population

While the threat of debris to operations in LEO currently is not acute, the trends are disturbing. In March 1983, two months after IRAS was launched, 5138 Earth orbiting objects were tracked by USSPACECOM radars. Only 5% of these objects were classified as operational payloads. The remaining objects were primarily non-operating satellites, satellite fragmentations and rocket stages and debris resulting from operational procedures (e.g. payload deployment). Over the last two decades about 120 new satellites have been launched per year, while the tracked population has increased by approximately 240 satellites annually (Johnson and McKnight 1987). As of 19 June 1991, 6883 objects of diameter 10 square centimeters and larger, were tracked by the USSPACECOM. The approximate number of operational payloads remained unchanged from the March 1983 value of 5%. Debris fragments accounted for 52.5% and spent rocket stages and non-operational payloads accounted for the remaining 42.5% (Anz-Meador 1991).

While the (former) USSR has accounted for 80% of the annual launch rate over the past decade, they only account for roughly 50% of the debris population. This is because many of their missions are designed to be short-lived and to re-enter the atmosphere within a few months. The US accounts for most of the remaining debris population. Contributions from other space faring nations are negligible. During periods of increased solar activity the debris population has remained constant or actually decreased because of increased atmospheric drag. As a result of this "self-cleaning" of the debris environment, the number of tracked satellites in orbit around the Earth is virtually the same in 1991 as it was in 1988.

It can not be ignored, however, that if the satellite population is allowed to increase unchecked, the probability of collisions between satellites will also continue to increase.

The greatest source of orbital debris is satellite fragmentations. Examination of the 1983 and 1987 USSPACECOM catalog of satellite orbital element sets (elsets) indicated that half of all space debris in orbit originated from the fragmentation of a satellite. Fragmentations are classified into three categories according to their cause: unknown (possible on-orbit collision), deliberate (e.g. alleged anti-satellite tests, disposition of sensitive equipment and structural testing) and hypergolic explosion (hypergolic fuel ignites on contact with oxidizer).

Unknown breakups account for 23% of the 103 satellites that have fragmented on-orbit since October 1991 (Rast 1991). Currently, there is only one satellite, Kosmos 1275, for which there is strong evidence that the fragmentation was the result of a hypervelocity impact from a piece of debris. The Kosmos 1275 breakup occurred in 1981 at an inclination of 83° and altitude of 1000 kilometers. It produced 249 pieces of debris that could be tracked by the USSPACECOM. Most of this debris is still in orbit (Johnson and McKnight 1987).

Three deliberate fragmentations were instigated by the US and include a structure test, the destruction of an ASAT target (the solar satellite SOLWIND) and a planned collision between a rocket body and a payload. The later occurred during an alleged Strategic Defense Initiative (SDI) testing program (Johnson and Nauer 1987). Most of the pieces from the first and last event have decayed. The only other fragmentations that were considered intentional were performed by the (former) USSR and were primarily ASAT

tests conducted prior to 1982. Historically, each deliberate fragmentation event has generated less than 100 pieces of debris eventually tracked by USSPACECOM.

Fragmentations that were the result of a hypergolic explosion have commonly generated hundreds of pieces of trackable debris. Computer simulations by the European Space Agency Orbital Debris Working Group (Rex 1990) have shown that between one and two thousand objects 1 millimeter and larger are generated in explosion events. Debris from a fragmentation event will initially remain in the same orbital plane as the parent satellite; however, it will be distributed around the Earth with other debris about the initial altitude over time by precession of the orbital plane (Rex 1990). Some of the most severe explosions have involved Delta booster second stages (Table 7)

Most operational satellites and debris from breakups can be found at altitudes near 800, 1000 and 1500 kilometers which implies that IRAS was well placed to observe orbital debris, particularly material generated by the explosions of Delta second stages. Future space based operations should consider carefully the level of acceptable risk in these altitude regions. This is particularly important for astronomical missions that may have sensitive instruments and mirrors exposed to the space environment.

2. Ground-Based Detection Systems

Surveillance of space debris in the United States comes under the jurisdiction of the USSPACECOM. This organization manages roughly 20 sensors, primarily radars, around the world. Observations are also made by other systems such as the Naval Surveillance System (NAVSPASUR), which monitors space objects as they pass over an electronic fence stretching across the US at a latitude of 33°, and interfere with a radio beam. Most

deep space satellites are monitored by passive optical detectors such as the Baker-Nunn cameras or by the Ground-based Electro-Optical Deep Space Surveillance system (GEODSS). This is because most ground based radars are limited in their detection capability to objects larger than a few centimeters in LEO. The GEODSS telescopes have a 2.1° field of view and are equipped with a 36 centimeter radiometer which measures light variations. All of these observations are routed to the Space Surveillance Center at Cheyenne Mountain in Colorado Springs where over 40000 observations are received and processed daily.

IRAS was a unique instrument with which to study orbital debris because it was a space-based system, operating across a wavelength regime that, due to atmospheric absorption and high backgrounds, is essentially inaccessible from the ground (limited ground-based observations can be done at 12 μm). Observations of centimeter-sized debris that can not be detected from Earth-based detection systems should be detected by IRAS.

3. Thermal Behavior of Artificial Satellites and IRAS Estimated Detection Capability

In order to determine the ability, compared with ground-based systems, of IRAS to detect artificial satellites and orbital debris, it is important to first understand the thermal behavior of objects in orbit around the Earth. Consider the idealized case of an isothermal object with no internal heat sources that is in thermal equilibrium with solar radiation and both reflected radiation and thermal emission from the Earth (Fig. 15). By the equation of

Sources of Radiation on a Space Vehicle in Earth Orbit
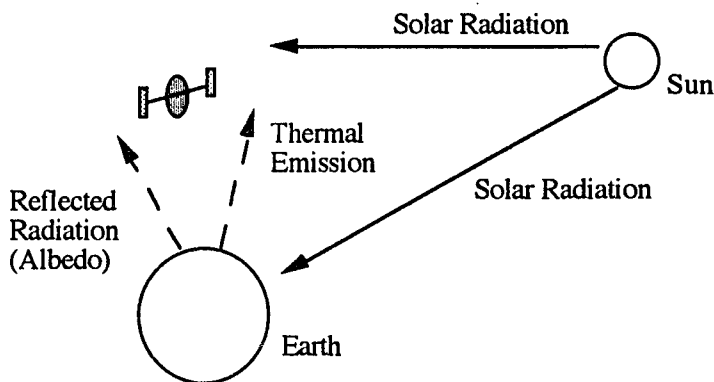
Figure 15: Satellites are irradiated from three sources: solar radiation and reflected radiation and thermal emission from the Earth. The contributions from of these sources vary with the distance and position of the satellite above the Earth, season and whether the object was in the Earth's shadow. The solar radiation incident on the upper atmosphere will vary by ±3% during the year due to the changing Earth-Sun distance. The mean-seasonal-average reflected radiation from the Earth, generally taken to be 36%, is a reasonable value between the latitudes of ±50°. The mean value of this parameter varies significantly over the surface of the Earth and depends on terrain, season and cloud cover. At the poles the value is closer to 70%. (Wolfe and Zissis 1978). It might prove useful to keep a meteorological record during the DCWS mission.

thermal radiative balance the total radiation absorbed by the object must equal the radiation emitted:

$$F_T \, A_a \, \alpha_s = \sigma T^4 \, \varepsilon_{ir} \, A_e$$

where: F_T = total incoming radiation = $[F_s + F_e + (\alpha_{th}/\alpha_s)F_{te})]$; between 200 and 2360 W m^{-2}; (Fig. 17)

F_s = solar radiation; between zero and 1400 Wm^{-2} d^{-2}(cos θ) χ

θ = solar elongation or "phase" angle between the Sun-Earth line and the Earth centered radius vector to the satellite. It varies between 81° and 99° for all sources observed by IRAS.

χ = percentage of time that the satellite is illuminated by the Sun. The procedure for determining χ can be found in the Appendix.3
d = distance from the Sun measured in AU

F_e = reflected radiation from the Earth's surface (also called albedo radiation); between zero and 560 Wm^{-2}

F_{te} = thermal emission from the Earth; between 200 and 400 Wm^{-2}

α_s = average solar absorptivity; fraction of incident radiation that is absorbed by a surface over the solar spectrum

α_{th} = average thermal absorptivity; fraction of incident radiation that is absorbed by the thermal spectrum; $\alpha_{th} \approx \varepsilon_{ir}$

ε_{ir} = average infrared emissivity; fraction of incident radiation that is reflected from a surface at infrared wavelengths

σ = Stefan-Boltzmann constant = 5.67 e -8 Wm^{-2} K^{-4}

T = mean temperature—K

A_e = area emitting radiation—m^2

A_a = area absorbing radiation—m^2

Note: The incoming radiation F_s and F_e are zero when an object is in the Earth's shadow. Under these circumstances F_{te} is the only source of input radiation.

Phase Angle of Objects Observed by IRAS
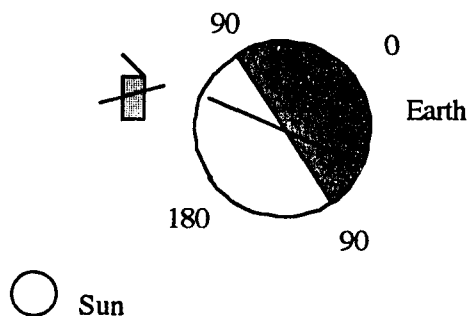
Figure 16: For sources observed by IRAS, the phase angle will always be close to 90° because IRAS orbited above the Earth's terminator. This means that when a source was observed by IRAS it was passing just into or out of the Earth's shadow. An object observed near the Earth's terminator will be either at its highest or lowest temperature (Lebofsky and Vilas 1990).

Solving for the thermal radiative balance equation for T:

$$T^4 = \frac{A_a\; \alpha_s\; F_T}{A_e\; \varepsilon_{ir}\; \sigma}$$

If the total incoming radiation is equal to the solar constant (1400 W m^{-2}), then the mean temperature for a flat plate and a sphere (Fig. 17) (improbable shapes for *most* satellites) equals:

$$T_{flat\;plate}\;(K) = [\pi r^2\; \alpha_s\; F_T\; /\; 2\pi r^2\; \varepsilon_{ir}\; \sigma]^{1/4}$$

$$[(F_T\; \alpha_s)\; /\; (2\; \varepsilon_{ir}\; \sigma)]^{1/4}$$

$$333.3\; (\alpha_s/\varepsilon_{ir})^{1/4}$$

$$C\; (\alpha_s/\varepsilon_{ir})^{1/4}$$

C = 204.9 to 379.8 K (for F_T = 200 to 2360 W m^{-2})

$$T_{sphere}\;(K) = [\pi r^2\; \alpha_s\; F_T\; /\; 4\pi r^2\; \varepsilon_{ir}\; \sigma]^{1/4}$$

$$[(F_T\; \alpha_s)\; /\; (4\; \varepsilon_{ir}\; \sigma)]^{1/4}$$

$$280.3\; (\alpha_s/\varepsilon_{ir})^{1/4}$$

$$C\; (\alpha_s/\varepsilon_{ir})^{1/4}$$

C = 172.3 to 319.4 K (for F_T = 200 to 2360 W m^{-2})

If the range of $\alpha_s/\varepsilon_{ir}$ is taken to be 0.1 to 10, which is typical for spacecraft materials, a sphere will have a temperature that ranges between approximately 158 K and 498 K and a flat plate will have a mean temperature between 187 K and 590 K. This assumes that the total incoming radiation is due to solar radiation. This calculation can be made more precise if the amount of reflected radiation and thermal emission received from the Earth, the duration in Earth's shadow and the phase angle are known.

<u>Flat Plate and Sphere Geometry</u>
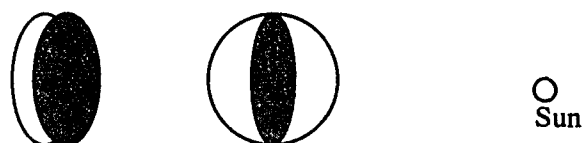
<u>Figure 17</u>: The shape of the satellite is important in determining its mean temperature. This figure shows the geometry of a flat plate and a sphere. For a thin flat plate, one side of the plate absorbs radiation and two sides emit radiation. A sphere will present one side, viewed as a flat plate, to the Sun; however, it will emit isotropically over its entire surface.

While it is instructive to examine the factors which dictate the thermal behavior of a satellite—incident sources of radiation, α_s, ε_{ir}, object geometry, Earth-Sun-satellite orientation and surface degradation, these parameters are complex and are not very amenable to a precise quantitative treatment. Still, it is evident from the above equations that the geometry of an object and the α_s and ε_{ir} values of spacecraft thermal control surfaces are of primary importance in regulating satellite temperatures.

Kirchoff's Law states that α is equal to ε at a given wavelength. With regard to satellites in Earth orbit, however, only the mean value of the solar absorptivity, α_s, and the mean value of the infrared emissivity, ε_{ir}, of a material are of interest. This is because objects in Earth orbit absorb radiation from the Sun and Earth at ultraviolet, visible and near-infrared wavelengths and emit radiation in the infrared. (The Sun emits 95% of its energy between 0.3 and 2.4 μm and a 300 K blackbody emits 95% of its energy between 3 and 40 μm.) Both quantities are dimensionless and vary between zero and one. Infrared emissivity is a weak function of surface temperature. A perfect emitter (a blackbody) has an emissivity of one; whereas, a material which has an emissivity that is independent of wavelength is called a graybody. It should be kept in mind that α_s and ε_{ir} can change as a function of lifetime, radiation exposure and handling before launch.

Throughout this discussion the term "absorptivity", α, is used instead of the term "albedo", a, (where $1-a = \alpha$). Albedo is a term that is used by astronomers and meteorologists to characterize the reflected solar radiation in a specified spectral region from a natural object such as a planet or an asteroid. Absorptivity is the term used by the aerospace community in all referenced publications when referring to artificial satellite components. It is suggested that the aerospace community convention be adopted when possible.

The detection capability of the IRAS detectors can easily be estimated and compared with other ground based detection systems (Fig 18a and 18b).

Defining the flux density from a source:

$$F_\nu(T) = \Omega\ \varepsilon_{ir}B_\nu(T)$$

where: $\Omega\ =\ \pi\ (r/R)^2 = $ solid angle subtended by the source

$F_\nu(T) = $ IRAS flux density detection limit
315 mJy for 12 μm detectors
375 mJy for 25 μm detectors

$B_\nu(T)\ = $ Planck function; the brightness of the source at frequency ν and temperature T

$$\frac{2h\nu^3\ c^2}{\exp(h\nu/kT)-1}$$

$$T^4 = \frac{A_a\ \alpha_s\ F_T}{A_e\ \varepsilon_{ir}\ \sigma}$$

$\therefore$ the distance to a source R for a given object radius r:

$$R^2 = \frac{B_\nu(T)}{F_\nu(T)}\ \pi r^2$$

Figure 18a and 18b: The estimated detection capability for the 12 and 25 µm passband detectors, as a function of altitude and diameter, for a non-rotating flat plate viewed face on. Detection limits for various values of α_s/ϵ_{ir} are shown. USSPACECOM radars are capable of seeing a baseball-sized object at an altitude of 500 kilometers. IRAS, on the other hand, could see the same size object, with the 12 µm passband detectors, up to ten times that distance. Size-range distance values derived from the above formula can be found in Appendix 2.

IRAS 12 Micron Estimated Detection Capability (3σ)
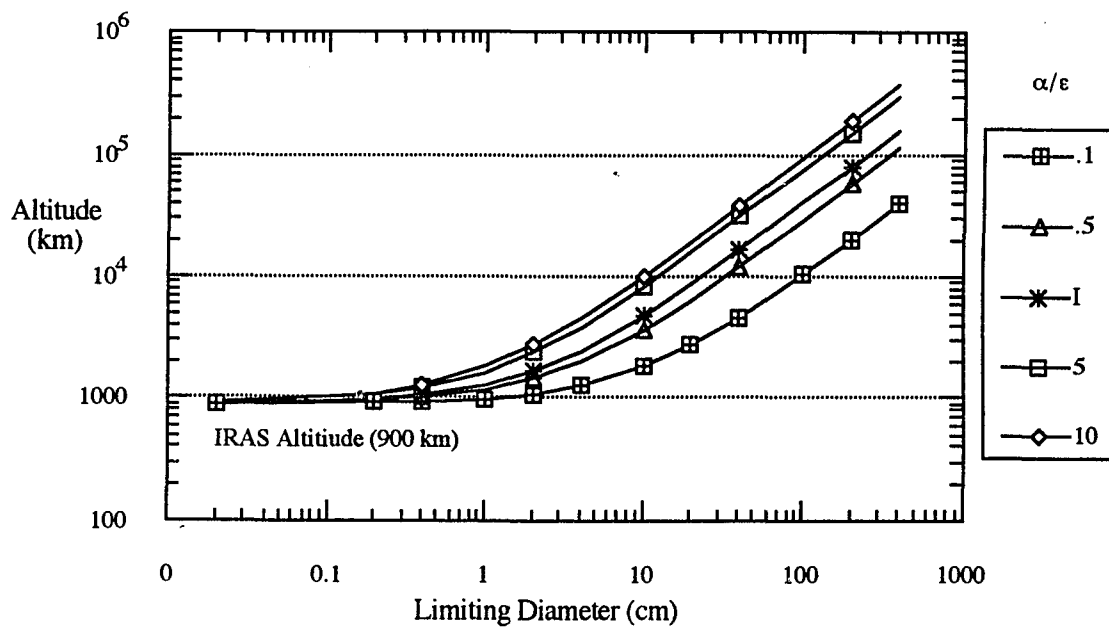
IRAS 25 Micron Estimated Detection Capability (3σ)
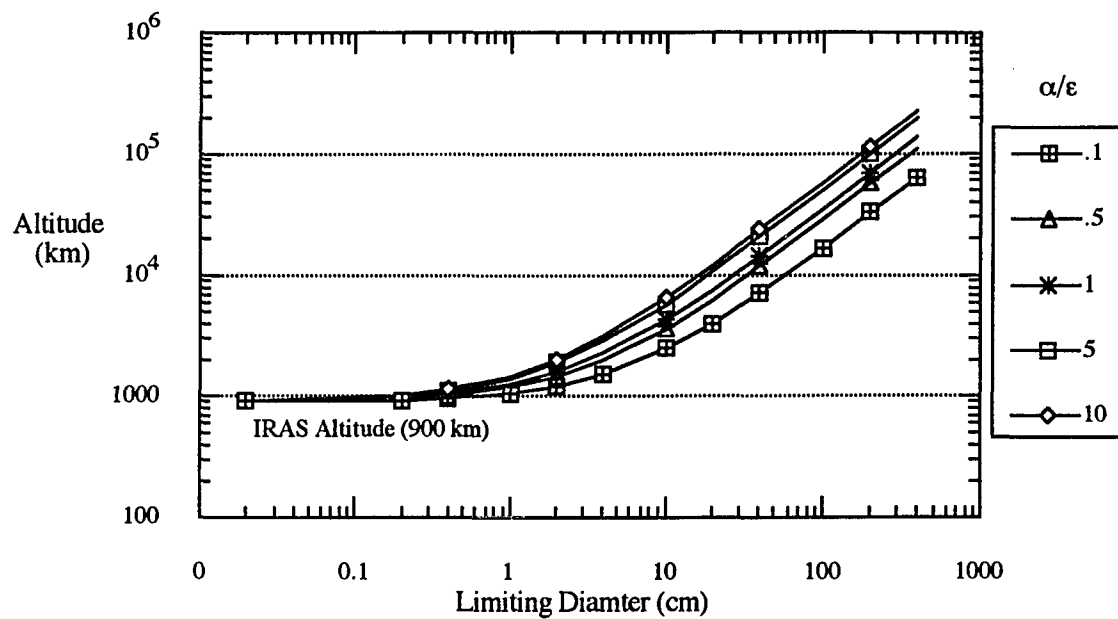
4. Spacecraft Materials

Some early studies of the thermal characteristics of debris assumed a value of 0.5 (Henize 1990) for albedo (equivalent to $\alpha = 0.5$) and 0.9 for emissivity—giving 0.55 for $\alpha_s/\varepsilon_{ir}$. Recent radiometry and photometry studies (Lebofsky and Vilas 1990), suggest that an albedo of 0.5 may be too high, because only the icy satellites of Jupiter and Saturn have albedos which are higher than this value. Examination of Table 6, however, indicates that most objects, with the exception of solar cells and black surfaces, actually have pre-launch albedos higher than 0.5 (α_s less than 0.5). While dark solar system objects such as asteroids are generally assumed to have an emissivity of 0.9 (e.g. Lebofsky and Spencer 1989), this is not the case for all satellites. Pre-launch emissivities of thermal control surfaces cover a wide range of values. While there is some evidence that debris particles become blackened as a result of the phenomena which created them (Vilas 1991), there remains a large population of objects in orbit that are not the result of a fragmentation event. An understanding of the thermal behavior of these payloads is equally important to the design of debris detection sensors for space based operations—in particular the space station Freedom.

When the ratio of the laboratory values of the α_s and the ε_{ir} of the most commonly used materials in spacecraft construction were examined, it was found that the range of $\alpha_s/\varepsilon_{ir}$ ranges between 0.1 to 10.0 and occasionally as high as 13.0 (e.g. Wolfe and Zissis 1978, Henninger 1984). This fact has important implications for the particle number and size distribution of the orbital debris environment. From the equation of thermal equilibrium:

$$F_T A_a \alpha_s = \sigma T^4 \varepsilon_{ir} A_e$$

$$\sigma T^4 = \frac{A_a\ \alpha_s\ F_T}{A_e\ \varepsilon_{ir}}$$

for a sphere:

$$\sigma T^4_{sphere}\ (K) = \frac{\pi r^2\ \alpha_s\ F_T}{4\pi r^2\ \varepsilon_{ir}}$$

$$= \frac{F_T\ \alpha_s}{4\ \varepsilon_{ir}}$$

Assuming $F_T = 1400\ W\ m^{-2}$:

$$\sigma T^4_{sphere} \propto \frac{\alpha_s}{\varepsilon_{ir}}$$

Since

$$\sigma T^4_{sphere} = L/4\pi r^2$$

where L = luminosity

$$r^{-2} \propto \frac{\alpha_s}{\varepsilon_{ir}}$$

For example, a particle with a diameter of one centimeter and an $\alpha_s/\varepsilon_{ir}$ of 0.5 will produce the same flux as a particle with a diameter of three centimeters if $\alpha_s/\varepsilon_{ir}$ is actually lower by a factor of 10.0. If $\alpha_s/\varepsilon_{ir}$ is really higher than 0.5 by a factor of 10, particles which were originally assumed to have a diameter of one centimeter will have a diameter of 0.3 centimeters. There is strong evidence that many objects have much higher values of $\alpha_s/\varepsilon_{ir}$ than previously assumed, which implies that many objects may be smaller than previously thought. It is imperative to know the values of $\alpha_s/\varepsilon_{ir}$ for small, untracked particles, such as white paint and solid rocket aluminum oxide effluents, if the population in this size regime

is to be modelled accurately. The DCWS flight experiment sensors have been designed with a mean albedo of 0.08 ($\alpha_s = 0.92$) and an emissivity of 0.9, or an α_s/ϵ_{ir} equal to 1.02, driving the experiment. If a paint flake observed by DCWS is assumed to have a diameter of one centimeter based on these values and the value of α_s/ϵ_{ir} is actually 0.28, the diameter of the particle will actually have been underestimated by a factor of two.

It is difficult to assign a mean value of the absorptivity (or albedo) or emissivity on all objects because debris has many different origins and surface properties. While there may be typical values within a certain size regime, small-sized debris may behave very differently, thermally, from operational payloads. The 0.08 value adopted for the DCWS design for the albedo is based soley on ground based optical observations (Henize 1990) of objects with diameters larger than 10 centimeters between the altitudes of 500 and 1100 kilometers. It is unknown if this value can be extended to other altituide regimes. The dispersion in albedo values determined by Henize (1990) is real as it should be. The very low albedo range, less than a = 0.12 (α_s = 0.88), is incomplete because there are so few materials which have an albedo in this regime. The high albedo range, between 0.2 - 0.8 (α_s = 0.8 - 0.2), includes many materials and may be incomplete because the objects with this albedo value may simply be harder to detect. While the above means values of albedo and emissivity may be useful in providing guidelines for the design of the DCWS, these values will not apply for all size regimes and all altitudes.

All objects in space, whether debris or components of operational payloads, can be classified four ways. Thermal control surfaces are considered to be either solar absorbers, solar reflectors, flat absorbers or flat emitters (Fig. 19). Solar absorbers, such as polished aluminum, have a high α_s and a relatively low ϵ_{ir} leading to a high temperature; whereas,

TABLE 6
Typical Solar Absorptivity and Infrared Emissivity Values for Spacecraft Materials

material	a	α_s	ε_{ir}	$\alpha_s/\varepsilon_{ir}$	T(1)	T(2)
AlO3 on Buffed Al	0.87	0.13	0.23	0.57	243	289
Vapor Dep. gold on glass substrate	0.96	0.04	0.02	2.00	333	396
Vapor Dep. silver on glass substrate	0.81	0.19	0.02	9.50	492	585
solar cell (IUE)	0.14	0.86	0.84	1.02	282	335
stainless steel (polished)	0.58	0.42	0.11	3.82	392	465
fiberglass	0.15	0.85	0.75	1.13	289	344
polished aluminum 6061	0.81	0.19	0.042	4.52	408	485
unpolished aluminum 6061	0.63	0.37	0.042	8.81	483	574
anodized aluminum	0.58	0.42	0.63	0.67	254	302
silver	0.96	0.04	0.02	2.00	333	396
gold (plated)	0.70	0.30	0.03	10.0	498	593
TiO white paint	0.80	0.20	0.90	0.22	192	228
black paint (3M Velvet Black)	0.05	0.95	0.92	1.03	282	336
aluminum paint	0.71	0.29	0.27	1.07	297	353
1.0 mil thickness Aluminized Mylar*	0.84	0.16	0.54	0.30	207	247
1.0 mil thickness silverized Teflon**	0.92	0.08	0.66	0.12	165	196
1.0 mil thickness aluminized Kapton***	0.64	0.36	0.54	0.67	254	302
Magnesium Oxide White Paint	0.91	0.09	0.90	0.10	158	187
Platinum Foil	0.67	0.33	0.04	8.25	475	565

*trade name fort polyethylene terephthalate
**trade name for fluorinated ethylene propylene
***trade name for polymide

T(1) = mean temperature of a flat plate
T(2) = mean temperature of a sphere
a = albedo
α_σ = solar absorptivity
ε_{ir} = infrared emissivity

Note: $\alpha_s/\varepsilon_{ir}$ values are taken from Wolfe and Zissis (1978), Wolfe (1965), Henninger (1984), and Wertz and Larson (1991).

Performance of Thermal Control Surfaces
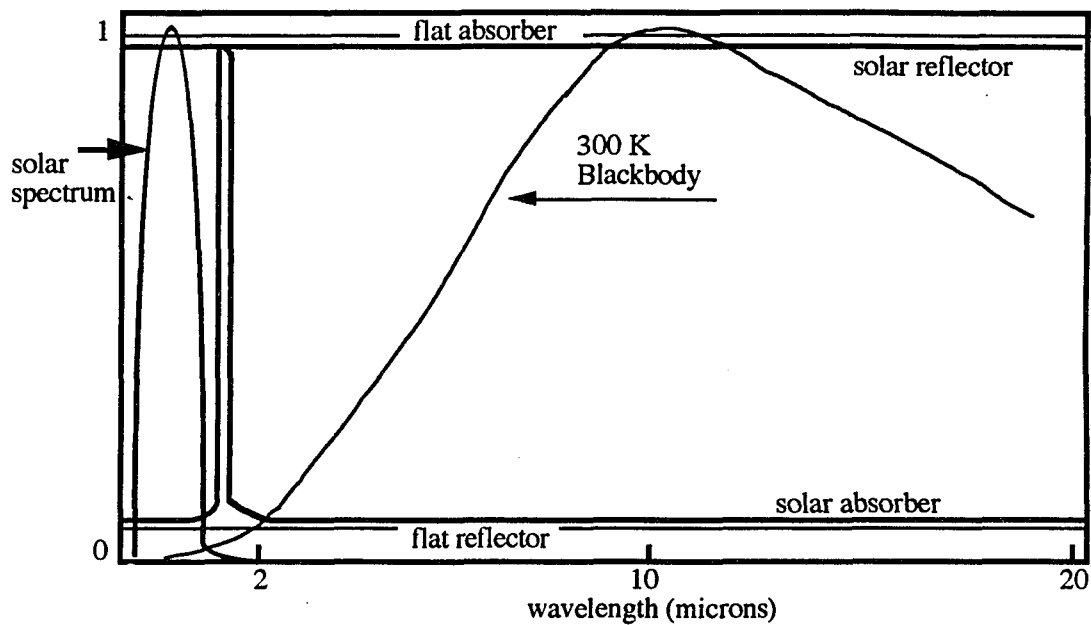
Figure 19: There are four types of thermal control surfaces: Flat absorber, flat reflector, solar absorber and solar reflector. Absorptivity to solar radiation should be small in order to make the response slow in going from shadow to sunlight.

solar reflectors, such as white paints have low α_s and high ε_{ir}, leading to a cool temperature. The flat absorbers, such as black paint, are essentially blackbodies because the α_s and the ε_{ir} both approach a value of one. Aluminum paint is an example of a flat reflector because it has a low absorptivity and a low emissivity.

Pre-launch laboratory measured values of $\alpha_s/\varepsilon_{ir}$ may not correspond exactly to actual values after exposure in space. The value of $\alpha_s/\varepsilon_{ir}$ can change dramatically with the thickness of a material, the condition of the surface and ultraviolet degradation. Published values of $\alpha_s/\varepsilon_{ir}$ should be used cautiously. Care must be exercised when handling thermal surfaces on the ground as scoring or fingerprints will also alter the value of $\alpha_s/\varepsilon_{ir}$. Some materials may also have a wavelength dependence. The emissivity of white and black paint, for example, decreases to about 0.2, from a value of roughly 0.9, between 50 μm and 75 μm where it decreases again to 0.1 at 100 μm (Kelly 1990). Values of α_s and ε_{ir} out to 20 μm are readily available in the literature and from the manufacturer of the material. The wavelength dependence of the emissivity of certain materials may be another explanation for the non-correlation between 12/25 μm and 25/60 μm color temperatures, particularly for sources with high apparent motions which may be best explained as paint flakes.

Extensive data on the effects of surface degradation does not exist at this time and it is not well understood how the values of $\alpha_s/\varepsilon_{ir}$ will change with lifetime. It is anticipated that ongoing studies of the Solar Max louvers and of the Long Duration Exposure Facility (LDEF) satellite will add much to our understanding of the degradation of satellite surfaces. Preliminary analysis of the LDEF surfaces indicate that there is evidence that α_s increases with time and that ε_{ir} remains relatively stable (Berrios 1991).

In January 1990, after almost 6 years in LEO, LDEF was by retrieved by the Space Shuttle. The primary surface coating on the spacecraft was chromic anodized aluminum which had a pre-launch α_s/ϵ_{ir} value equal to 0.32/0.26. One of the primary purposes of the mission was to measure the effects of the LEO space environment on spacecraft thermal control coatings. Thirty-three percent of the vehicle was measured and it was found that anodized aluminum is a very stable surface in the LEO environment. The value of α_s changed by no more than 16% and the value of ϵ_{ir} did not change significantly from their pre-launch values. The exact amount of change in the values of α_s depend on the location on the spacecraft as the satellite always pointed in the same direction relative to the Sun. White paint on the other hand showed varying degrees of degradation with some increases as much as 100%. The use of white paint as a thermal control surface may therefore subject a spacecraft to unwanted thermal excursions.

5. Correlation of Sources with Artificial Satellites

The sources that have very high angular motions, and thus are quite close to the IRAS focal plane, may be associated with the one of several satellite fragmentation events. Seven Delta second stage propulsion-related fragmentations occurred between 1973 and 1981. With one exception, all of these Delta rockets were launched from Vandenberg AFB into Sun-synchronous orbits. The cause of these events has been determined to be hypergolic fuel ignition (Johnson and Nauer 1987). The cataloged debris from the Delta failures alone accounted in 1983 for 14% of the entire catalogued population. Other fragmentation events have occurred near altitudes of 900 kilometers in near-polar orbits. The Nimbus-4 Agena rocket body and the Kosmos 1275 payload breakups, due to unknown causes, were two of the worst fragmentation events prior to 1983. The events listed in Table 7 accounted in 1983 for 25% of the entire population of tracked payloads and debris in Earth orbit.

To correlate objects observed by IRAS with known artificial satellites, the monthly updated USSPACECOM two-line elsets were acquired for the 10 months of the IRAS mission. The catalog contains the basic orbital elements for each object in orbit around the Earth and is current as of the date that the catalog was generated. A software package called SATRAK (Satellite Tracking 1989), developed by Teledyne Brown Engineering for the US Air Force, was used to propagate the satellite orbits to a date and time when a satellite passed in front of the IRAS focal plane. A window of 5° centered on the IRAS boresight, and a time interval of one minute centered on the observation time were used in the propagation routine. Orbits propagated beyond 30 days are unreliable and therefore sightings which did not have a corresponding elset within that time could not be correlated.

Of the fourteen sources with the lowest angular motions, three were determined to be asteroids and three have properties similar to asteroids but could not be correlated, using IPAC developed software, with known asteroids. Of the remaining eight sources, four were correlated with known astronomical satellites. One source could not be propagated because an elset within a 30 day epoch was not available. The four sources which were correlated include the final stage of a Soviet rocket, the payload ATS 6, an Atlas-Centaur rocket body associated with the US payload Intelsat, and the payload FTV-ERS. The other three sources did not match any cataloged satellite and are either satellites with unavailable or no current elsets. There are approximately 300 satellites in orbit whose elsets fit this description. For example, 40 of the 315 satellites in geosynchronous orbit, are classified as "lost" and another 30 have "unavailable" orbital elements (Johnson and Nauer 1987).

TABLE 7*
Rocket Body Fragmentations Before 1983

Satellite	Inc (deg)	Breakup Altitude (km)	Event Date	#Frag. Cat.	#Frag.in orbit (1987)	Period (min)
Nimbus-4 Agena Rocket	99.8	1076	8 Apr. 1970	344	291	106.7
NOAA-3 Delta Rocket	102.0	1513	28 Dec. 1973	184	168	116.2
Landsat-1 Delta Rocket	98.3	725	22 May 1975	226	89	100.3
NOAA-4 Delta Rocket	101.7	1460	20 Aug. 1975	139	131	114.9
Landsat-2 Delta Rocket	97.8	751	9 Feb. 19 Jun 1976	200	50	101.0
NOAA-5 Delta Rocket	102.0	1510	24 Dec. 1977	142	141	116.3
Landsat-3 Delta Rocket	98.9	905	27 Jan. 1981	194	172	103.
Kosmos 1275 payload	82.9	977	24 Jul. 1981	282	278	104.8

*(Johnson and Nauer1987)

SL-6 Booster (Final Stage)

Source 373 was correlated using SATRAK with an SL-6 (US designation) booster final stage. In the 1960's the SL-6 supported all planetary missions and many lunar flights. Today it is used primarily in conjunction with early warning and communication satellite programs. It is the third most commonly used Soviet booster (Johnson 1990). This particular booster launched the early warning payload Kosmos 1409. The booster is cylindrical in shape and has a height of 3.2 meters and is 2.4 meters in diameter. It was painted yellow, green or white, in that order of likelihood, (Rast 1991) and has an inclination of 65°

Source 373 passed in front of the IRAS focal plane with an angular motion relative to the satellite of 5.3 arc-minutes/ second. It was observed at the position RA = 12:26:47 Dec = -28:34:06 on 20 July 1983. The SL-6 final stage was determined to have a color corrected temperature of 280 K.

Applications Technology Satellite (ATS-6):

The ATS-6 payload (Fig.20) was correlated with Source 305 using SATRAK. The satellite consisted of a central Earth Viewing Module which was 1.4 x 1.4 meters at the base and 1.67 meters high. A parabolic antenna nine meters in diameter formed a structure of 48 aluminum ribs which were covered by copper netting treated with dacron and silicon. ATS-6 was launched 30 May 1974 on a Titan III-C rocket into an orbit of

ATS-6 Payload
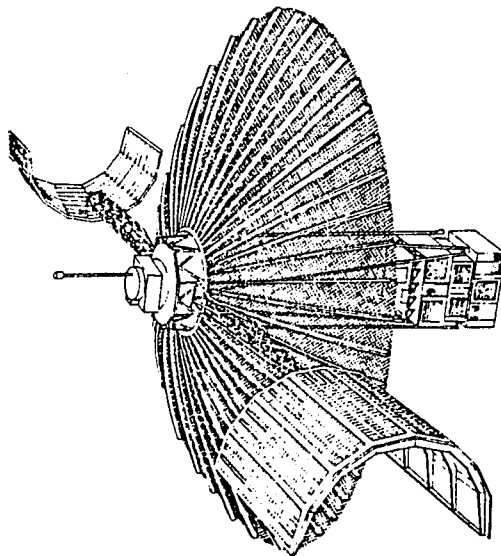
Figure 20: ATS-6 was the sixth satellite in the Applications Technology Satellites series. It was launched 30 May 1974 by a Titan III-C rocket and remained operational for five years.

inclination 8°. The color corrected temperature from the IRAS data was determined to be 274 K.

The angular motion of Source 305 determined from the CRDD was 4.46 arc-minutes/second compared to 4.63 arc-minutes/second as predicted by SATRAK. ATS-6 was seen by IRAS on 3 November 1983 at a range of 34300 kilometers above the focal plane at RA = 20:48:32 and Dec -04:09:14. The position of ATS-6 relative to the IRAS boresight as predicted by SATRAK differs by less than one minute in RA and by roughly six minutes in Dec with the position determined from the Sky Brightness Image. As the position from the Sky Brightness Image may not necessarily coincide with the boresight, the positional agreement is excellent given the dimensions of the focal plane.

Intelsat 4A Rocket Body

Source 282 is correlated with the Intelsat 4A Atlas Centaur rocket body and was obseved by IRAS at RA = 08:41:22 Dec +06:58:31 on 28 April 1983. The rocket body was observed at a range of 16600 kilometers from the IRAS focal plane and has a color corrected temperature of 325 K. The angular motion predicted from the CRDD was 5.26 arc-minutes/second. The rocket body passed over the focal plane 1 minute and 27 second later than predicted by SATRAK. The angular motion at this time was 5.19 arc-minutes/second. As there is good agreement between the two angular motion predictions, this is considered a correlation. The Intelsat rocket body has an inclination of 20° and is in a highly eccentric orbit .

FTV-ERS 10

The FTV-ERS 10 payload was correlated with Source 228. It was observed by IRAS on 7 July 1983 at a range of 2970 kilometers. Launched on 18 July 1963, it has been in orbit longer than any of the other satellites which were correlated in this study. It is in an orbit inclined 88°. The SATRAK generated position for the time specified agrees with tthe CRDD position to within a few seconds in RA and to within 17 minutes in Dec. The SATRAK angular motion is 5.27 arc-minute/second at the time of observation, which is in good agreement with the 5.07 arc-minute/second angular motion calculated from the CRDD. This payload has a color temperature of 323 K.

Summary of Chapter Three

The orbit chosen for IRAS was one of the best positions from which to observe payloads and debris. Since studies by other investigators have found few objects in the CRDD and since there are only a few hundred artifacts on the Sky Brightness Images, it can be inferred that using the de-glitcher was an effective means of eliminating debris from the data stream.

The detection capabilities of space-based telescopes like IRAS far exceed the ability of ground-based systems to detect debris. While a dedicated space-based debris detection system such as the DCWS will provide the most reliable information about debris in many size regimes, the thermal properties of the most frequently used spacecraft materials should be understood before the results from such a program are analyzed. Given the LDEF results, it would seem that less effort should be placed on ground-based observations of operational satellites, and more effort placed on researching the thermal control surfaces

which have been used on objects already placed into orbit. This type of information is readily available from the manufacturers of satellites and launch vehicles (Fig. 21).

Delta Second Stage Thermal Control Surfaces

STANDARD DELTA II 2ND STAGE
PASSIVE THERMAL CONTROL REQUIREMENTS

RF SHIELD
  • Anodized Aluminum
      $\alpha/\varepsilon = .42/.63$

GUIDANCE SECTION
  • White paint exterior $\alpha/\varepsilon = .3/.9$

AFT CONICAL GUIDANCE SECTION
  • Green primer exterior
      $\alpha/\varepsilon = .9/.9$

FUEL TANK
  Side Wall (cylinder)
  • MLI on cylinder (code 1) $\alpha/\varepsilon = .13/.6$

  Aft Tank (conical)
  • MLI on aft conical section (code 2)
  • Low ε foil on aft dome
      $\alpha/\varepsilon = 13/.6$

ENGINE SECTION
  • MLI (code 3)
      $\alpha/\varepsilon = .13/.6$
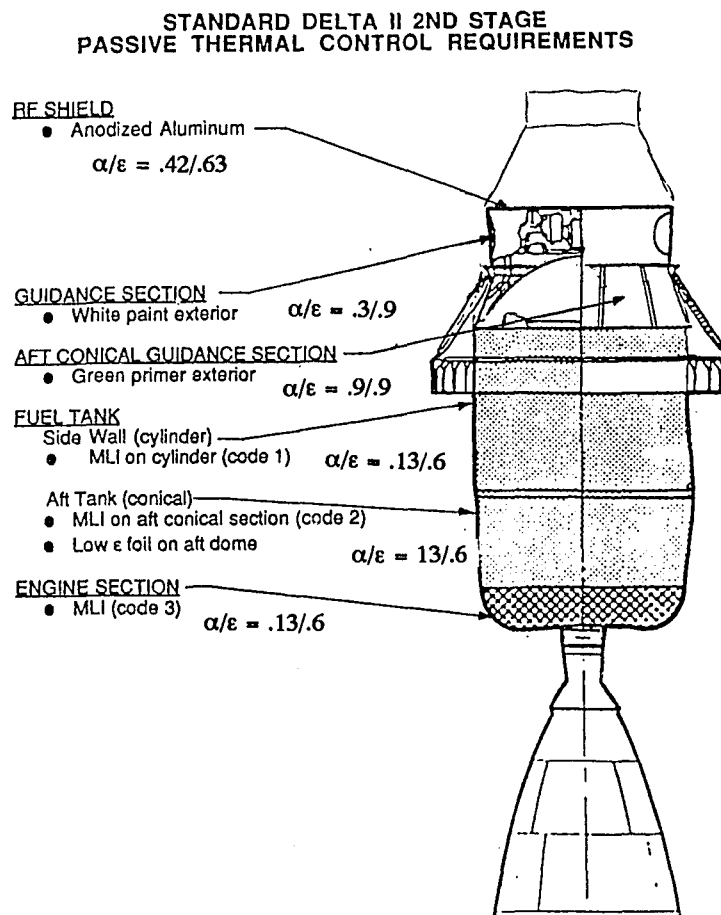
Figure: 21: This schematic of a Delta second stage indicates the different thermal control surfaces on the vehicle. Residual hypergolic propellants in the second stage tanks are thought to be the prime energy source in the fragmentation of seven Delta second stages.

Summary

Space debris is an environmental problem. Although great strides have been made towards understanding the thermal behavior and distribution of this debris, it has only been in the past decade that a means of controlling and decreasing the population have been seriously addressed by NASA, ESA, COSPAR and the IAU.

The debris situation is of interest to ground-based and space-based astronomy. Images taken with wide-field CCD detectors may contain satellite trails. As many as nine trails appear on a given plate of the second-generation Palomar Observatory Sky Survey (Reid 1991). For now, this is only a cosmetic problem, as military jets flying in formation and air traffic near Los Angeles International Airport actually pose a greater annoyance. Shara and Johnston (1986) have calculated that the Hubble Space Telescope has a 1% chance of being destroyed by a piece of debris with a diameter greater than 10 centimeters and a 50% chance of being damaged by debris during the spacecraft's anticipated 17 year lifetime. Given that the spatial density of payloads and debris is lower here than in the heavily populated regions containing Sun-synchronous orbits between 800 and 1200 kilometers, one wonders what fate awaits IRAS or the Cosmic Microwave Background Explorer

Astronomical missions should be familiar with the distribution of the present debris population and with models that predict the future situation. Designers of space-based satellites should investigate the need for debris avoidance and shielding as part of mission planning. Additionally, debris mitigation methods should be incorporated into future satellite designs to avoid further compromising of the space environment.

This study of Earth orbiting objects observed by IRAS has demonstrated that, while detecting orbital debris from a space-based platform is a complex problem, it is currently the most reliable means of learning about a population of objects which is both diverse in both size and composition. Our understanding of these characteristics will undoubtedly increase as future experiments such as the DCWS are launched.

Appendix 1
Detections

column 1: source number
column 2: Sky Brightness Image number
column 3: HCON
column 4: relative visual intensity from 1 (high) to 3 (low)
column 5: direction from which passband detections are ordered (N,S,E,W) in column 6
coulum 6: order of detections on Sky Brightness Image
column 7: Right Ascension (1950)
column 8: Declination (1950)
column 9: diameter of source on Sky Brightness Image in arc-seconds

```
 1    1 1 1   12301230  22h31m14s   87d15m57s  40
 2    1 2 1     123113  20h38m12s   80d24m24s  40
 3    1 2 1          0  22h48m48s   84d20m49s  52
 4    1 3 1   33213221  13h40m21s   81d57m21s  40
 5    1 3 1     321321   5h42m29s   83d28m33s  24
 6    1 3 2         12  10h20m37s   82d 6m57s  20
 7    2 1 0          0   0h 0m 0s    0d 0m 0s   0
 8    2 2 2      32321  22h 9m19s   77d30m 9s  28
 9    2 2 2     321321  22h53m16s   70d42m57s  28
10    2 3 1      32321  22h35m42s   74d58m 9s  24
11    2 3 1     321321   1h53m25s   75d 0m 2s  36
12    2 3 1        321   0h 8m43s   72d13m24s  24
13    2 3 0          0  22h35m31s   75d 0m 1s  28
14    2 3 0          0  22h36m 0s   75d 0m42s  40
15    3 2 2     123123   0h20m 8s   78d21m55s  32
16    3 2 1     123123   1h27m40s   74d12m54s  32
17    3 2 1     123123   1h39m15s   72d35m22s  36
18    3 3 1      32133   1h54m 9s   74d56m41s  24
19    3 3 1          0   1h 0m10s   79d11m17s   0
20    3 3 1          0   3h40m45s   80d10m42s   0
21    4 1 3      12323   6h51m56s   81d31m27s  36
22    4 1 3      12213   5h 9m51s   61d13m12s  36
23    4 1 3      12123   5h26m13s   72d54m37s  36
24    4 2 1      12313   4h57m10s   72d15m19s  28
25    4 2 1         23   4h37m48s   68d38m24s  16
26    5 1 1     121233   8h10m35s   67d48m27s  40
27    5 1 2        123   7h40m48s   68d22m21s  16
28    5 1 2      12323   6h52m10s   81d32m23s  36
29    5 1 2        123   7h34m43s   81d15m55s  16
30    5 1 1        123   9h27m26s   77d24m26s  28
31    5 1 3      12132   5h25m38s   72d54m59s  36
32    5 2 1      12312   8h51m46s   77d53m35s  36
33    6 1 2     123213  10h 0m19s   69d12m41s  36
34    6 3 1    3321331  10h 6m19s   75d42m48s  32
35    6 3 3       3313   8h33m 6s   68d55m34s  36
36    7 1 2       3211   9h45m34s   77d26m35s  36
37    7 1 2      12313  11h55m42s   68d13m41s  32
38    7 2 1    3221321  13h15m34s   71d 2m57s  44
39    7 2 1        321  12h38m21s   68d15m 5s  20
40    7 3 1   11223123  13h38m 3s   81d51m49s  40
41    7 3 1     321321  13h56m39s   76d 5m26s  28
42    8 1 1     321321  14h 7m18s   68d34m29s  40
43    8 1 1     321321  16h12m13s   77d31m56s  36
44    8 2 1     321321  13h15m14s   71d 2m48s  40
45    8 2 1     321321  13h 6m53s   65d54m30s  28
46    8 2 2      32121  16h 5m15s   80d17m30s  24
47    8 3 1     321321  13h56m48s   76d 4m20s  28
48    8 3 2     123123  16h 4m27s   79d15m23s  28
49    8 3 1     123123  13h40m16s   81d57m 9s  36
50    9 1 1     321321  16h12m 2s   77d32m59s  36
51    9 1 2       2232  16h38m33s   71d55m18s  36
52    9 2 2      32121  16h 4m40s   80d14m47s  24
53    9 2 3     321321  17h37m 2s   74d56m17s  36
54    9 2 3       3322  17h24m35s   70d24m40s  16
```

```
 55    9 3 1     13123  16h 5m 3s   79d14m25s  32
 56   10 1 1       233  19h30m33s   68d11m59s  20
 57   10 1 2     31321  17h50m26s   68d37m 6s  32
 58   10 2 2   1123113  20h37m49s   80d27m35s  36
 59   10 2 2     11232  19h51m58s   78d25m27s  32
 60   10 2 3    321321  17h37m24s   74d57m13s  32
 61   10 2 3    123113  21h54m 9s   79d28m40s  36
 62   10 3 1      2313  20h32m18s   75d43m54s  28
 63   11 1 0         0   0h 0m 0s    0d 0m 0s   0
 64   11 2 2   1112312  19h52m30s   78d18m49s  36
 65   11 2 1  33213321  21h52m47s   73d51m32s  40
 66   11 2 2      3232  22h 9m25s   77d32m11s  24
 67   11 3 1      3132  20h32m18s   75d40m17s  24
 68   11 3 0         0  21h 0m10s   76d45m35s  40
 69   11 3 0         0  22h 0m10s   76d15m34s  24
 70   14 1 3     12312   3h 5m27s   60d43m24s  28
 71   14 2 3     31211   2h38m47s   54d49m41s  40
 72   14 3 1     12233   3h18m 6s   64d11m 4s  36
 73   15 1 3        23   5h 7m36s   57d58m23s  16
 74   16 2 2   1231223   6h 6m49s   62d15m56s  36
 75   16 2 3       313   6h31m17s   65d12m28s  32
 76   16 3 2    313221   7h25m35s   58d36m36s  32
 77   16 0 0         0   6h14m32s   54d51m26s  44
 78   17 1 3    123312   8h21m58s   62d33m25s  28
 79   17 1 3     12331   7h14m45s   56d23m13s  28
 80   17 2 3      2312   8h34m50s   65d25m51s  32
 81   17 2 2      1213   6h58m51s   58d 4m52s  32
 82   17 2 3        32   7h36m47s   54d42m30s  12
 83   17 3 2    313221   7h25m42s   58d34m52s  36
 84   18 1 3    123123  10h42m 1s   65d 0m 4s  32
 85   18 3 3    321321   9h26m14s   53d18m19s  20
 86   19 1 2    123123  10h41m45s   65d 1m40s  32
 87   19 1 3       123  11h39m38s   54d46m58s  20
 88   19 2 2    213221  11h 3m 1s   62d34m49s  40
 89   19 2 3       123  11h18m 3s   58d 5m30s  16
 90   19 3 3     32321  11h13m21s   54d15m 7s  28
 91   20 2 2     31321  12h25m51s   60d47m 9s  36
 92   20 2 1    123123  13h 6m31s   65d54m30s  36
 93   21 2 1    321321  13h 7m 1s   65d55m35s  36
 94   21 3 1     12323  14h44m33s   63d 2m13s  32
 95   21 3 1       123  14h33m53s   58d18m35s  16
 96   22 1 1     12313  16h 1m33s   64d45m18s  40
 97   22 1 2       322  16h43m28s   56d43m41s  16
 98   22 2 1      3213  16h32m33s   57d50m23s  32
 99   22 2 1     12313  16h48m44s   59d31m57s  36
100   22 2 2      1213  16h15m14s   58d20m37s  16
101   22 2 2       321  15h17m23s   55d10m34s  16
102   22 3 2     12323  16h44m30s   55d 0m 0s  32
103   23 1 3       323  18h 1m55s   60d44m36s  20
104   23 1 3       322  16h43m29s   56d44m34s  16
105   23 2 1      1233  16h49m11s   59d28m34s  36
106   23 2 3       321  16h58m43s   59d26m 4s  16
107   23 3 3    123123  16h44m45s   54d59m58s  32
108   23 3 1     12313  17h32m28s   60d31m49s  36
```

109	23 3 1		12331123	17h24m32s	60d44m 9s	36
110	24 1 2		32332321	19h 2m16s	66d44m58s	40
111	24 1 1		3232211	20h 7m20s	66d 0m59s	40
112	24 2 0		1233333	19h40m53s	64d38m44s	40
113	25 1 2		32231211	20h 7m28s	66d 0m28s	40
114	25 1 0		0	20h38m 8s	64d26m13s	0
115	25 3 1		212	21h12m35s	66d28m59s	16
116	26 3 1		321	22h 8m55s	52d 3m18s	20
117	27 1 3		32121	23h59m39s	40d 8m41s	32
118	27 1 2		123	0h 7m13s	52d56m 5s	12
119	28 1 2		23213	0h56m27s	39d 7m19s	36
120	28 1 2		31321	1h22m36s	50d19m15s	24
121	28 1 3		3212	11h33m15s	45d24m35s	16
122	28 2 2		11211	0h47m12s	42d40m 0s	28
123	28 2 3		321	0h42m 4s	43d53m19s	16
124	29 1 2		32321	1h59m34s	46d36m12s	32
125	30 1 3		121233	3h59m32s	44d 2m55s	20
126	30 1 3		1123	4h 9m42s	45d59m20s	12
127	30 1 3		123	4h 0m34s	43d26m 7s	16
128	30 3 1		321	4h 9m 7s	43d22m 1s	20
129	31 3 1		3121	4h 9m15s	43d19m22s	28
130	31 3 2		223	4h26m19s	40d 3m 6s	12
131	31 3 1		223	4h31m12s	38d40m58s	16
132	33 3 1		12312321	6h42m32s	45d 9m45s	24
133	34 3 1		332132221	8h58m26s	42d12m41s	36
134	34 3 1		321321	9h 4m 1s	50d 1m 5s	36
135	35 3 1		123123	9h27m 5s	45d20m41s	28
136	35 3 1		321321	9h 4m25s	49d59m 0s	36
137	35 3 1		321321	8h58m18s	42d14m49s	36
138	36 2 1		321	10h27m20s	40d39m32s	24
139	36 2 1		123123	10h54m22s	46d19m19s	32
140	37 2 1		123123	12h18m36s	37d21m10s	40
141	38 2 2		1213	13h46m21s	39d53m33s	24
142	38 2 2		1231	13h14m30s	42d 2m 3s	20
143	39 1 2		1231233	14h16m33s	48d32m49s	32
144	39 2 1		1231233	14h 7m49s	47d33m37s	40
145	39 2 3		323	14h15m12s	49d24m13s	24
146	39 2 1		2313	13h46m 9s	39d57m25s	20
147	39 2 3		123	14h 6m31s	41d45m13s	12
148	39 3 3		12313	14h 2m52s	50d 7m55s	28
149	40 1 2		12313	14h 4m34s	51d17m14s	36
150	40 3 3		12331123	15h42m23s	38d 3m23s	36
151	41 3 2		12331123	16h 4m50s	51d18m12s	32
152	41 1 2		231	16h13m43s	50d39m47s	20
153	41 1 3		12321123	16h10m25s	40d 5m40s	40
154	41 1 1		12321123	16h44m 2s	47d39m37s	40
155	41 1 3		11223133	16h32m 4s	41d16m10s	40
156	41 2 3		11223123	16h27m38s	41d51m24s	28
157	41 2 2		2331313321	17h31m24s	50d22m20s	40
158	41 3 2		12312	16h12m48s	49d51m 7s	28
159	41 3 3		123123	16h11m20s	40d34m34s	28
160	41 3 3		1321	17h 3m52s	39d44m47s	16
161	42 1 3		321	18h23m42s	39d55m39s	16
162	42 2 3		33331	17h31m30s	50d21m52s	36

```
163  42 2 3     31313 17h24m26s  45d53m14s 40
164  42 3 1    112313 17h41m15s  50d59m 0s 32
165  43 1 1         0 19h25m37s  47d36m51s 32
166  43 3 1      2323 18h56m33s  47d45m58s 24
167  45 1 2     33213 22h 2m38s  39d 7m43s 24
168  45 1 2        11 21h55m 8s  39d40m58s 12
169  45 2 2        32 21h58m46s  39d16m43s 24
170  45 3 2     12123 22h 8m24s  51d58m56s 32
171  45 3 3    122312 22h23m17s  51d53m42s 28
172  46 1 3      1321 23h 7m31s  44d47m45s 32
173  46 2 1   3213211 22h 0m33s  47d48m52s 24
174  46 2 3    321321 22h54m 6s  47d25m18s 32
175  46 2 0         0  0h 0m 0s   0d 0m 0s  0
176  46 3 1    132121 22h 8m 6s  51d58m10s 40
177  46 3 1    321321 22h23m20s  51d54m10s 36
178  47 1 1    321321 23h39m36s  26d48m41s 36
179  47 1 3       121 23h50m42s  35d27m39s 24
180  47 2 1       321 23h28m52s  26d 5m42s 16
181  48 2 1    321321  1h22m44s  35d19m 0s 24
182  48 2 1    321332  1h26m50s  34d24m22s 40
183  48 2 3    321321  1h 8m27s  33d30m39s 20
184  48 2 2    321321  0h55m37s  34d52m59s 32
185  49 1 1        32  1h56m52s  31d21m50s 12
186  49 2 1    213233  1h26m47s  34d22m28s 40
187  49 2 1    321321  1h22m35s  35d21m 6s 28
188  49 3 3  32131232  1h41m45s  26d19m56s 28
189  49 3 3    321321   2h 7m 6s  34d36m37s 32
190  49 3 2        32  2h15m40s  28d56m35s 12
191  51 1 3     12323  3h45m53s  29d39m11s 36
192  51 1 2      1233  4h33m54s  31d52m57s 20
193  51 2 3  12231223  3h56m39s  24d13m 2s 28
194  51 2 3    121323  4h35m56s  32d46m27s 20
195  56 1 1      1321  9h37m54s  33d49m38s 32
196  56 3 2     32321  9h27m11s  25d36m59s 32
197  57 1 1      3221  9h37m37s  33d48m 2s 20
198  57 2 1   1233123  9h52m12s  25d17m51s 28
199  57 2 2    123123 10h30m17s  35d12m48s 24
200  57 3 1   3321321 10h17m56s  36d31m11s 40
201  57 3 1     32321  9h26m58s  25d38m24s 32
202  58 2 1    123123 10h30m11s  35d11m16s 32
203  58 3 2       321 11h21m14s  35d51m40s 12
204  59 1 1   1231233 12h18m37s  37d23m56s 32
205  60 1 3     12312 13h24m 4s  34d12m39s 32
206  60 2 1     12323 13h11m30s  24d23m26s 32
207  61 1 2     12312 13h23m59s  34d11m35s 32
208  61 1 3       213 14h12m41s  25d48m22s 16
209  62 1 3    213213 15h 0m44s  26d28m15s 16
210  62 1 3       113 14h38m54s  23d40m 7s 32
211  62 2 2    123123 14h50m59s  30d50m49s 16
212  62 3 2      1231 15h32m59s  26d27m54s 24
213  62 0 2         0 14h27m28s  24d59m19s 68
214  63 1 1     12313 16h18m 3s  31d15m14s 36
215  63 1 1         0 16h 9m52s  22d33m22s 56
216  63 3 2      1231 15h33m 2s  26d24m43s 24
```

```
217  63  3  3      3123  15h54m 5s   33d37m10s  32
218  64  1  2      3211  16h55m57s   30d51m45s  20
219  64  2  1    321331  17h 2m 4s   33d17m43s  32
220  64  2  1      1321  17h 1m33s   31d13m57s  24
221  64  3  2       123  16h28m42s   33d52m40s  12
222  65  3  2      2323  18h27m33s   36d51m52s  32
223  66  2  3       321  19h19m 9s   28d 9m 1s  16
224  66  3  2    123123  18h27m42s   36d49m21s  36
225  69  1  2        21  22h 5m13s   32d51m26s  16
226  70  1  2     32131  22h37m58s   24d44m46s  20
227  70  2  1       321  23h28m47s   26d 7m31s  16
228  71  2  1       321  23h34m48s   22d 4m27s  20
229  71  2  2      1213  23h40m 8s   21d 6m12s  16
230  71  2  3     32321   0h 0m58s   17d53m50s  20
231  71  2  3     31321  23h56m46s    9d 7m11s  32
230  71  2  3     32321   0h 0m58s   17d53m50s  20
231  71  2  3     31321  23h56m46s    9d 7m11s  32
232  73  1  2    321321   2h 2m55s    7d12m51s  32
233  73  2  3      1321   1h40m24s    9d25m 0s  24
234  73  2  3       323   1h44m19s   12d34m22s  16
235  74  1  2   1233131   3h 2m 9s    9d25m 2s  32
236  75  1  3         0   3h51m10s   -1d14m56s   0
237  77  3  1       132   5h46m 9s   18d 1m58s  12
238  78  1  2        23   7h20m29s   20d28m26s  16
239  78  2  2      1233   7h31m 1s   13d 7m 1s  20
240  78  2  3    123123   8h 1m22s   14d43m59s  32
241  78  3  2     12312   6h42m36s   13d43m43s   0
242  79  1  2    123123   8h11m11s   10d13m56s  28
243  79  2  1      3321   7h30m59s   13d 7m54s  24
244  79  2  3    123123   8h12m39s    7d29m53s  32
245  80  3  0         0   9h24m34s   19d17m17s   0
246  80  3  3      3321   9h 8m 4s   16d59m21s  20
247  82  2  1     12323  11h27m55s   12d 4m53s  20
248  82  2  1    123123  11h31m30s   11d47m38s  28
249  83  1  2      1231  12h 5m28s   18d47m22s  24
250  83  2  1     12313  11h38m27s    9d55m 0s  32
251  83  2  2    123123  11h31m26s   11d44m50s  32
252  83  2  1     12323  11h27m55s   12d 3m12s  24
253  83  2  1    123123  12h30m 8s   15d26m19s  28
254  84  1  2       123  12h48m35s    9d 0m38s  20
255  84  2  2    123123  12h30m 8s   15d24m28s  28
256  86  1  1  12231233  14h57m26s    9d50m48s  32
257  86  1  3     12313  15h12m23s   16d58m32s  28
258  86  0  0         0  14h35m18s    8d34m37s  40
259  87  2  1     12313  16h13m11s   16d34m24s  36
260  87  2  1       222  15h30m29s   11d52m23s  32
261  88  1  1    321321  17h18m14s   10d52m23s  40
262  88  3  2   1231233  17h15m22s   18d 1m32s  28
263  89  1  2      3121  18h 3m11s   16d 7m54s  32
264  89  1  3      2121  18h 6m32s    7d34m19s  24
265  89  2  1    323321  17h51m17s   11d59m39s  36
266  90  2  2    332131  19h 8m44s   19d24m41s  20
267  90  2  1       211  18h55m53s   20d22m51s  20
268  90  3  3       123  18h40m 4s   14d26m51s  16
```

```
269   91 2 1    3221321 20h 0m16s   17d51m51s 36
270   92 1 1     321321 20h53m19s   12d19m48s 36
271   92 1 2      13212 21h 4m41s    8d43m24s 20
272   92 3 3        123 21h 5m 9s   11d30m 5s 16
273   94 1 0          0 22h41m19s   19d 6m 1s  0
274   98 1 0          0  3h19m49s    2d55m11s 28
275   98 2 0          0  3h31m39s   -3d43m31s 32
276  100 2 0          0  5h13m58s    5d30m21s 28
277  101 3 3       2121  6h20m 4s   -1d19m40s 32
278  102 1 3     123123  6h47m12s    4d31m 0s 32
279  103 1 3      12312  8h 4m39s    0d43m59s 28
280  104 1 3     321321  8h55m52s   -1d 9m58s 28
281  104 1 3        123  9h29m26s   -1d15m21s 12
282  104 1 3        123  8h41m22s    6d56m33s 12
283  104 3 2        222  8h57m52s    3d33m 4s 12
284  105 1 3        212  9h40m 3s    5d27m45s 12
285  105 2 3       2322  9h41m30s    4d54m18s 24
286  106 2 3        232 11h 5m 3s    0d27m59s 12
287  108 1 1       3121 13h 4m 7s    5d13m 4s 28
288  108 2 2        122 12h44m33s   -5d28m14s 20
289  108 2 2        212 12h57m52s   -2d 5m56s 16
290  110 1 3        321 15h 3m59s   -4d59m11s 12
291  110 3 2      12323 15h 8m15s    0d 7m59s 32
292   11 1 2     123123 15h44m 1s    0d11m58s 24
293  111 2 3        123 15h36m44s   -2d45m 1s 20
294  112 2 3   33213321 17h17m49s    5d 8m14s 28
295  112 3 2        123 16h56m48s    1d13m58s 16
296  113 1 2       2121 18h11m27s    0d13m58s 20
297  114 1 1   32133211 19h13m 3s    5d40m19s 32
298  114 3 1         12 18h39m31s    5d43m28s 12
299  114 3 1         12 18h36m36s    6d18m28s 12
300  115 3 1       1231 20h 4m31s    0d19m59s 24
301  115 3 1        123 19h43m 5s   -7d 0m44s 20
302  116 2 2     123123 20h54m48s    4d11m29s 24
303  116 3 2      23313 20h58m48s    3d51m38s 28
304  116 3 2        123 20h51m28s    2d45m45s 12
305  116 3 3        123 20h48m32s   -4d 9m14s 16
306  118 1 1        321 23h10m15s    5d22m43s 16
307  118 2 2        231 23h29m26s    1d47m 4s 24
308  120 1 2        321  0h51m58s  -15d27m27s 16
309  120 1 1       3213 01h15m53s  -09d53m24s 16
310  121 1 3     321321  2h20m 6s  -16d24m23s 32
311  121 2 2     321321  2h24m12s  -10d11m18s 28
312  121 2 1     321321  2h10m25s  -10d53m45s 20
313  121 2 0     321321  1h35m45s  -14d 3m27s 28
314  122 1 2     321321  3h13m 8s  -13d18m45s 24
315  122 2 1        321  2h44m49s  -22d52m15s 16
316  122 2 2     322321  3h 7m 0s   -9d42m38s 24
317  122 2 1     321321  2h50m 4s  -20d47m43s 36
318  122 2 1       2121  3h19m 9s  -22d44m46s 32
319  122 2 3      31321  3h14m54s   -9d25m52s 28
320  122 3 1       3121  2h53m20s  -16d 5m36s 32
321  124 1 1     123123  4h55m59s  -14d51m52s 28
322  124 1 1      11312  5h11m32s  -21d42m37s 28
```

```
323 124 2 1      122   4h41m26s -20d47m 1s 32
324 125 1 1     2323   5h57m21s -16d59m53s 28
325 126 1 2    12123   6h45m46s -13d20m32s 32
326 126 1 2   123123   7h31m 5s -21d 5m47s 20
327 126 3 1      213   7h 4m31s -20d 8m56s 16
328 127 1 2    12123   8h19m16s -22d29m 2s 28
329 127 1 2       23   7h56m45s -10d38m26s 12
330 127 2 1   231321   8h30m24s -21d10m11s 24
331 127 2 1  1231223   8h22m13s -20d55m15s 32
332 127 3 1    31321   8h23m54s -21d59m17s 32
333 128 1 2   231321   8h49m55s -18d 0m51s 28
334 128 2 1   321321   8h30m34s -21d10m50s 24
335 128 2 3    12323   8h30m28s -15d58m23s 16
336 130 2 1   123123  10h46m24s  -9d39m55s 36
337 131 1 1    12323  12h24m26s -13d27m34s 24
338 132 2 2    12312  13h14m36s -10d59m 4s 28
339 137 2 2      123  17h43m41s  -8d20m32s 12
340 138 1 2        0  18h44m56s -11d26m49s 44
341 138 1 2      122  18h56m 5s -17d19m46s 12
342 139 2 3   321321  19h48m59s -14d23m 2s 16
343 141 2 0        0  22h11m58s -24d34m51s 40
344 145 2 0        0   1h54m38s -23d41m11s 36
345 146 1 0        0   2h49m24s -29d40m25s 24
346 146 2 0        0   2h54m16s -30d25m31s 24
347 146 2 0        0   2h45m11s -23d 3m25s 28
348 146 2 0        0   3h19m11s -22d45m56s 36
349 147 1 0     2323   4h24m25s -36d50m30s 32
350 147 2 0        0   3h43m59s -24d23m53s 28
351 147 2 3        0   3h30m14s -23d24m58s 32
352 148 0 0        0   5h18m 8s -37d32m 4s 36
353 149 3 1   321321   5h35m19s -24d51m 9s 32
354 149 3 1   331321   6h24m 6s -37d30m 2s 36
355 150 3 1   321321   6h40m 6s -31d48m 9s 36
356 150 3 3   321321   6h46m28s -32d11m13s 32
357 150 3 2    31321   6h24m 0s -37d28m29s 28
358 151 2 1     3123   8h30m35s -28d45m 1s 24
359 152 1 1     1212   9h20m20s -24d17m59s 24
360 152 2 1     3123   8h30m36s -28d46m 0s 24
361 152 3 1      321   9h12m 8s -34d51m 1s 20
362 152 3 1      321   8h40m45s -28d32m55s 24
363 153 2 1    32122   9h53m40s -37d20m55s 32
364 153 2 2    12313  10h33m53s -32d44m37s 28
365 154 2 1   123123  10h38m11s -28d31m28s 32
366 154 2 3    12313  10h33m56s -32d45m41s 28
367 154 2 2       22  11h 0m54s -28d49m59s 16
368 154 1 2   123123  10h54m24s -30d47m32s 40
369 154 1 3      132  10h29m25s -35d34m15s 12
370 155 1 2     1232  12h26m56s -28d34m 0s 12
371 156 1 2       32  12h50m14s -32d12m31s 16
372 156 1 3   121123  12h29m 9s -36d23m16s 28
373 156 1 3      323  12h26m55s -28d32m52s 12
374 156 2 2     3123  12h34m 7s -22d42m25s 24
375 157 1 1    12331  14h11m10s -34d53m21s 24
376 157 1 1   123313  13h42m10s -35d 2m17s 32
```

```
377 157 2 1   1231223 14h37m18s -34d41m45s 36
378 158 1 1     12313 15h26m40s -35d31m48s 24
379 158 3 2      2332 14h41m 5s -29d56m55s 36
380 158 3 2   2333232 14h36m45s -23d38m58s 40
381 159 1 2     12313 15h26m53s -35d27m47s 40
382 161 1 2        12 18h12m58s -30d23m35s 20
383 162 3 3    123123 19h29m32s -24d39m56s 40
384 163 3 3     12123 19h29m45s -24d35m28s 40
385 169 0 0         0  2h17m19s -39d12m28s  0
386 170 1 0    321321  4h 1m44s -42d47m12s 40
387 170 1 0    321321  3h27m53s -50d18m 1s 40
388 175 2 3      3212  9h53m37s -37d25m39s 28
389 175 2 3    312312 10h 4m 3s -40d 1m55s 36
390 176 2 1    333322 11h24m49s -50d22m49s 24
391 177 2 1       332 11h24m50s -50d42m46s 16
392 177 3 1    123123 12h40m12s -51d49m51s 40
394 178 1 3   1231223 12h52m43s -41d48m 7s 32
394 178 1 2      3123 13h33m10s -39d37m39s 24
395 178 3 1    123123 12h40m 5s -51d51m33s 36
396 179 1 3    123223 14h33m 4s -40d36m27s 32
397 179 1 3    123123 13h41m17s -44d31m59s 36
398 179 3 2    123123 14h 0m14s -45d56m44s 28
399 182 1 1     21312  0h 0m 0s   0d 0m 0s 32
400 182 3 2       212 17h51m 6s -48d50m21s 24
401 182 3 2      1212 18h18m11s -44d 6m35s 24
402 183 1 1        19 19h38m51s -46d50m 8s 32
403 183 1 1     32121 19h33m 4s -52d32m13s 24
404 183 3 1       231 18h27m 1s -47d26m40s 28
405 184 1 1   2211233 19h53m 3s -47d54m10s 32
406 184 1 2   1233123 19h45m26s -43d53m33s 36
407 184 2 3       121 20h13m15s -43d 0m 9s 32
408 185 2 2     12123 21h54m30s -44d32m23s 40
409 185 2 2    321321 22h15m46s -45d 7m58s 40
410 186 2 0    123123 22h15m44s -45d 6m55s 40
411 186 2 3   3321211 23h24m28s -48d27m58s 40
412 187 3 0      3123 23h45m17s -58d16m51s 40
413 188 1 2    321321  1h44m48s -56d 3m11s 40
414 188 2 2      3121  2h28m 7s -66d13m18s 40
415 188 2 3     31321  2h 5m51s -54d41m 0s 40
416 188 2 2    321321  2h 0m58s -56d40m49s 40
417 188 3 0      3213  2h14m 8s -56d44m16s 40
419 189 2 0         0  3h 6m50s -62d17m34s  0
420 189 2 0         0  3h 7m24s -62d19m38s  0
421 189 2 0         0  3h 7m41s -62d21m40s  0
422 190 0 0         0  5h11m 8s  60d16m27s 32
423 191 0 0         0  6h18m34s -66d59m33s 24
424 193 2 3      1231  8h50m54s -55d41m15s  0
425 194 1 3    112312 11h12m27s -54d17m 8s 32
426 194 3 3     32321 10h37m49s -54d36m43s 32
427 195 1 2     31233 12h17m19s -59d24m 5s 28
428 195 3 2       132 12h33m50s -55d 5m37s  0
429 198 1 1       213 18h 9m48s -53d41m26s 28
430 198 1 2    321321 18h 0m36s -53d18m12s 32
```

```
431 198 1 1       321 17h32m54s -67d25m22s 24
432 198 2 3    321321 18h25m42s -52d 6m55s 24
433 198 2 1    321321 18h35m21s -62d56m55s 40
434 199 1 2      1332 19h37m54s -52d55m26s 24
435 199 1 1     32132 19h25m54s -61d21m19s 40
436 199 1 1       321 19h33m 4s -52d31m25s 24
437 199 2 1    332321 18h35m19s -62d57m57s 40
438 199 2 2    321321 18h25m44s -52d 6m20s 28
439 199 3 3    123123 19h37m 6s -62d29m26s 28
440 200 2 2       221 21h21m41s -56d55m 7s 24
441 204 1 0         0  2h41m12s -77d35m 5s  0
442 204 2 0         0  5h32m25s -74d57m51s  0
443 204 2 0         0  4h19m16s -70d30m 0s  0
445 205 0 0         0  7h40m 1s -70d 0m26s  0
446 209 1 2       321 17h32m39s -67d27m 8s 20
447 209 1 2    321321 16h13m25s -70d38m12s 32
448 209 1 1    312321 18h10m57s -73d45m54s 40
449 209 2 2      1321 17h45m 9s -67d24m 9s 20
450 209 2 2    321321 17h 9m21s -72d33m48s 40
451 209 2 2     21321 16h12m19s -69d41m15s 20
452 209 2 1     32321 15h32m10s -71d31m47s 40
453 209 2 1     21321 18h 5m26s -77d53m46s 20
454 209 2 1      2121 18h 3m24s -81d47m36s 28
455 209 3 2    123123 17h12m 5s -68d21m12s 28
456 209 3 2    123123 15h38m35s -70d59m47s 28
457 209 3 1      1231 14h53m27s -77d41m30s 20
458 209 3 2    123123  17h 0m54s -76d14m43s 36
459 210 1 2    321321 18h11m22s -73d45m48s 28
460 210 2 2      3213 20h11m37s -75d21m38s 40
461 210 3 0    123123 17h 1m11s -76d14m51s 40
462 210 3 0    321321 20h55m 6s -75d13m 2s 20
463 211 1 1    321321 20h55m25s -75d16m46s 20
464 211 1 2      3313 22h16m 7s -73d43m51s 20
465 211 2 2      3213 20h12m 9s -75d22m 9s 40
```

Appendix 2				
IRAS Detection Capabilty				

IRAS 12 μm Detection Capability 3σ				
Limiting Diameter cm	Distance km			
	$\alpha_s/\varepsilon_{ir} = 0.1$	$\alpha_s/\varepsilon_{ir} = 0.5$	$\alpha_s/\varepsilon_{ir} = 1.0$	$\alpha_s/\varepsilon_{ir} = 5.0$	$\alpha_s/\varepsilon_{ir} = 10.0$
0.02	901.90	905.61	907.96	914.98	918.58
0.20	919.03	956.14	979.64	1049.80	1085.76
0.40	938.05	1012.28	1059.29	1199.60	1271.52
1.00	995.14	1180.69	1298.22	1649.00	1828.81
2.00	1090.27	1461.39	1696.43	2398.00	2757.62
4.00	1280.54	2022.78	2492.86	3895.99	4615.25
10.00	1851.36	3706.94	4882.16	8389.98	10188.12
20.00	2802.71	6513.88	8864.31	15879.97	19476.24
40.00	4705.42	12127.76	16828.62	30859.94	38052.47
100.00	10414.56	28969.40	40721.56	75799.85	93781.18
200.00	19927.11	57038.81	80543.11	150699.70	186662.40
400.00	38954.23	113177.6	160186.20	300499.40	372424.70

IRAS 25 μm Detection Capability 3σ				
Limiting		Distance		
Diameter		km		
cm				
$\alpha_s/\varepsilon_{ir} = 0.1$	$\alpha_s/\varepsilon_{ir} = 0.5$	$\alpha_s/\varepsilon_{ir} = 1.0$	$\alpha_s/\varepsilon_{ir} = 5.0$	$\alpha_s/\varepsilon_{ir} = 10.0$
0.02	901.90	905.61	907.96	914.98	918.58
0.20	919.03	956.14	979.64	1049.80	1085.76
0.40	938.05	1012.28	1059.29	1199.60	1271.52
1.00	995.14	1180.69	1298.22	1649.00	1828.81
2.00	1090.27	1461.39	1696.43	2398.00	2757.62
4.00	1280.54	2022.78	2492.86	3895.99	4615.25
10.00	1851.36	3706.94	4882.16	8389.98	10188.12
20.00	2802.71	6513.88	8864.31	15879.97	19476.24
40.00	4705.42	12127.76	16828.62	30859.94	38052.47
100.00	10414.56	28969.40	40721.56	75799.85	93781.18
200.00	19927.11	57038.81	80543.11	150699.70	186662.40
400.00	38954.23	113177.60	160186.20	300499.40	372424.70

Appendix 3
To Determine the Percentage of an Orbit χ that is illuminated by the Sun

$a = 1.38 \times 10^6 \text{ km}$ $d = 1.5 \times 10^8 \text{ km}$

Earth

not to scale   Sun
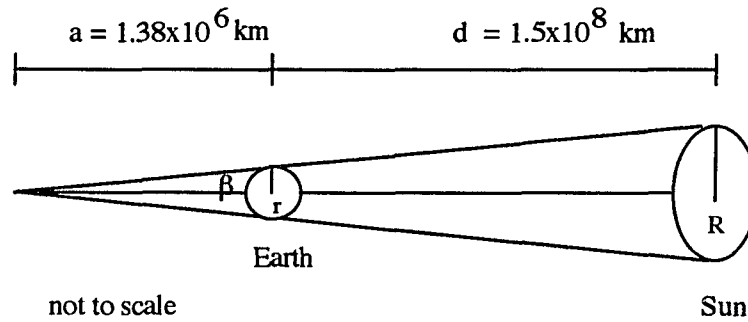
$\tan \beta = r/a = R/(a+d)$

$\tan \beta = 6378.16 \text{ km}/a = 6.96 \times 10^5 \text{km} / (a + 1.50 \times 10^8 \text{ km})$

$\therefore a = 1.38 \times 10^6 \text{ km}$

$\tan \beta = 6378.16 / 1.38 \times 10^6 \text{km}$

$\beta = 4.61 \times 10^{-3} \text{ rad}$

$\beta = 0.26°$

$2\beta = 0.5°$

(Approximately 1.9% of this circular orbit is in the Earth's shadow)

Geosynchronous satellites are located roughly 6.67 Earth radii from the center of the Earth:

$\tan \beta = 6378.16 / 6378.16 \ (6.67)$

$2\beta = 17.06°$

(A maximum of 4.8% of a geosynchronous satellite's orbit will be spent in the Earth's shadow.)

Appendix 4
To Determine the Altitude of a Source Observed by IRAS

n = true angular motion of a satellite in orbit as seen from the center of the Earth
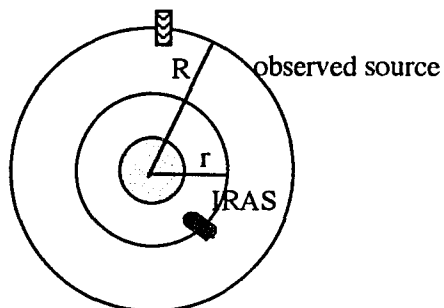
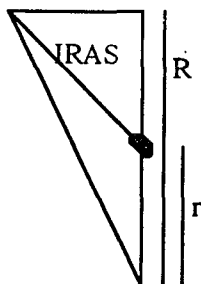$$= (GM/R^3)^{1/2}$$ where   R=semi-major axis of the Earth

M=mass of the Earth

n_{iras} = 3.5 '/s = the angular motion of IRAS as seen from the center of the Earth

n_{scan} = 3.85 '/s = the scan rate of the IRAS satellite

Assume you are in a rotating frame of reference—ie IRAS is motionless above the Earth. The angular motion of the satellite as seen from the center of the Earth is $n - n_{iras}$.

Since IRAS is closer , the apparent angular motion of the satellite as seen from IRAS (over small angles) is :

$$(n - n_{iras}) [R/(R-r)]$$

In the rotating frame, IRAS is scanning at a rate:

$$n_{scan} - n_{iras} = 3.85 '/s - 3.5 '/s = 0.35 '/s$$
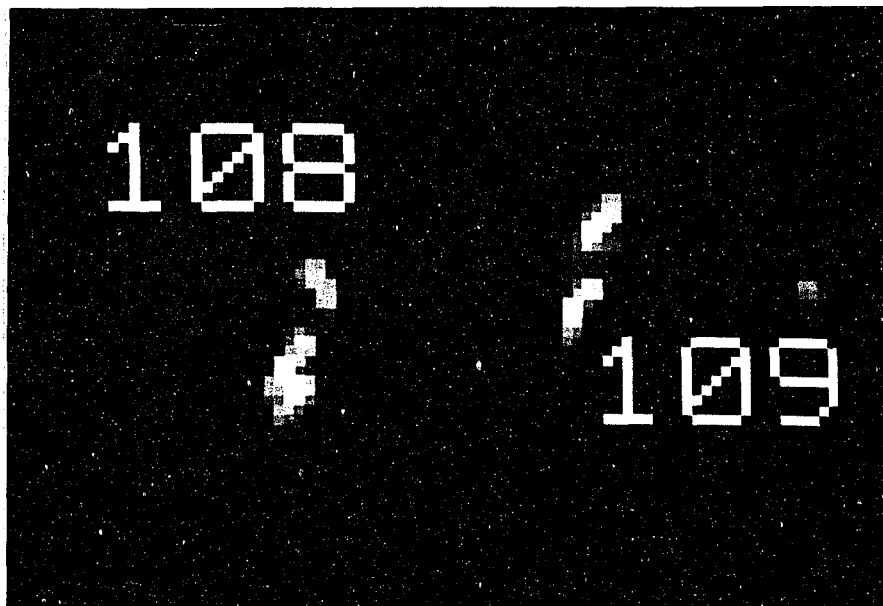
So, the apparent rate of satellite motion n' across the IRAS detector plane is :

$$n' = \text{scan rate in rotating frame} - \text{angular motion as seen from IRAS}$$

$$n' = (n_{scan} - n_{iras}) - [(n - n_{iras}) (R/R-r)]$$

$$n' = 0.35 '/s - [(n - 3.5 '/s)(R/R - (6378 km + 900km))]$$

$$n' = 1.02e-4 rad/s - [(n - 1.02e-3 rad/s)(R/R-7278 km)]$$

Appendix 5
Photographs of Earth Orbiting Objects Observed by IRAS

References

Anz-Meador, P.D., 1991, private communication

Anz-Meador, P.D., 1992, private communication

Anz-Meador, P. D., Oro, D.M., Kessler, D.J.and Pitts, D.E., 1986, Advances in Space Research 6:139

Berrios, W.M., 1991, private communication

Chester, T., 1991, private communication

deJong, A.R.W. and Wesselius, P.R., 1990, AIAA/NASA/DOD Orbital Debris Conference Proceedings, Baltimore, MD

Dow, K.L. and Sykes, M.V., 1988, Bull. Am. Astr. Soc. 19:1070

Dow, K.L., Sykes, M.V., Low, F.J. and Vilas, F, 1990, Adv. Space Res., v.10, no. 3-4, pp 381

Flury, W., 1988, "Space Debris, A Report from the ESA Space Debris Working Group,' ESA Publications Division, ESTEC. Noordwijk, The Netherlands

Gautier, N., 1989, private communication

Henize, K, 1990, AIAA/NASA/DOD Orbital Debris Conference Proceedings, Baltimore, MD

Henninger, J.H., 1984, Solar Absorptance and Thermal Emittance of Some Common Spacecraft Thermal Control Coatings, NASA Reference Publication 1121, April 1984

IRAS Catalogs and Atlases: Explanatory Supplement. 1988, ed, C.A. Beichman, G. Neugebauer, H.J. Habing, P.E. Clegg and T.J. Chester (Washington, D.C.: GPO)

IRAS Point Source Catalog, Version 2 1988, Joint IRAS Science Working Group (Washington, D.C.: GPO)

IRAS Small Scale Structure Catalog, 1988, prepared by G. Helou and D. Walker (Washington, D.C.: GPO)

IRAS Sky Brightness Images, 1988, as described in the IRAS Explanatory Supplement 1988

Johnson, N.J., 1990, 'The Soviet Year in Space', Teledyne Brown Engineering, (Colorado Springs, Colorado)

Johnson, N.J. and Nauer, D.J., 1990, AIAA/NASA/DOD Orbital Debris Conference Proceedings, Baltimore, MD

Johnson, N.L. and Nauer, D.J., 1987, 'History of On-Orbit Satellite Fragmentation', *Technical Report*, Third Edition, Teledyne Brown Engineering, Colorado Springs, Colorado.

Johnson, N.L. and McKnight, D.S. 1987, Artificial Space Debris, Orbit Book Co: Malabar FL

Kelly, T., 1990, private communication

Lebofsky, L.A., Sykes, M.V., Tedesco, E.F., Veeder, G.J., Matson, D.L., Brown, R.H., Gradie, J.C., Feierberg, M.A. and Rudy, R.J., 1986, Icarus, 68:239

Lebofsky, L.A., and Spencer,1989,.Radiometry and Thermal Modelling of Asteroids, In Asteroids II, eds. Binzel,, R.P., Gehrels, T. and Matthews, M.S., Tucson: University of Arizona Press

Lebofsky, L. and Vilas, F., 1990, Adv. Space Res., v.10, no. 3-4

Low, F.J., 1991, private communication

Maley, P., Astrophysical Journal (Letters), 1987, 317:L39

Neugebauer, G.*et al.*. 1984, Astrophysical Journal (Letters), 278:L1

Pouw, A. 1983, Journal of the British Interplanetary Society, 36:17

Rast, R., 1991, private communication

Ried, N., 1991, private communication

Satellite Tracking (SATRAK),1989, Colorado Springs, CO: Teledyne Brown Engineering

Shara, M and Johnston, M.,1986, Artificial Earth Satellites Crossing the Field of View of and Colliding with, Orbiting Space Telescopes, Publications of the Astronomical Society of the Pacific, 606:814

Sykes, M.V., Lebofsky, L.A., Hunten, D.M. and Low, F.J., 1986, Science, 232:1115

Sykes, M.V.and Walker, R., 1992, Icarus, 95:180

Tedesco, E.F., 1989, Asteroid Magnitudes, UBV Colors, and IRAS Albedos and Diameters, In Asteroids II, eds. Binzel,, R.P., Gehrels, T. and Matthews, M.S., Tucson: University of Arizona Press

Vilas, F., 1991, private communication

Vilas, F., 1992, private communication

Walker, R.G., Matson, D.L. and Veeder, G.J., 1986, Adv. in Space Res., vol. 6, no.7

Walsh, L., Wesselius, P. R. and Olthof, H., 1989, 40th Congress of the IAF, IAA-89-629

Wertz, J.R. and Larson, W.J., (eds.), 1991, Space Mission Analysis and Design, Kluwer Academic Publishers, Dordrecht

Wolfe, W.L and Zissis, G.J., (eds.), 1978, The Infrared Handbook, Office of Naval Research, Department of the Navy, Washington, D.C.

Wolfe, W.L., (ed), 1965, Handbook of Military Infrared Technology, Office of Naval Research, Department of the Navy, Washington, D.C.